

The ~ 0.9 mJy sample: A mid-infrared spectroscopic catalog of 150 infrared-luminous, 24 micron selected galaxies at $0.3 \leq z \leq 3.5$

Kalliopi M. Dasyra¹, Lin Yan², George Helou^{1,2}, Anna Sajina³, Dario Fadda², Michel Zamojski¹, Lee Armus¹, Bruce Draine⁴, David Frayer²

ABSTRACT

We present a catalog of mid-infrared (MIR) spectra of 150 infrared (IR) luminous galaxies in the *Spitzer* extragalactic first look survey obtained with the IR spectrograph on board the *Spitzer* Space Telescope. The sample is selected to be brighter than ~ 0.9 mJy at 24 μm and it has a redshift distribution in the range $[0.3, 3.5]$, with a peak at $z=1$. It primarily comprises ultraluminous IR galaxies at $z \gtrsim 1$ and luminous IR galaxies at $z < 1$, as estimated from their monochromatic rest-frame 14 μm luminosities. The number of sources with spectra that are dominated by an active galactic nucleus (AGN) continuum is 49, while 39 sources have strong, star-formation related features. For this classification, we used the equivalent width (EW) of the 11.3 μm polycyclic aromatic hydrocarbon (PAH) feature. Several intermediate and high z starbursts have higher PAH EW than local ULIRGs, which is indicative of an elevated star formation activity. Moreover, an increase in the AGN activity is observed with increasing z and luminosity, based on the decreasing EW of PAHs and the increasing $[\text{Ne III}]/[\text{Ne II}]$ ratio. Spectral stacking leads to the detection of weak features such as the 3.3 μm PAH, the H₂ 0-0 S(1) and S(3) lines, and the [Ne V] line. We observe differences in the flux ratios of PAHs in the stacked spectra of IR-luminous galaxies with redshift or luminosity, which cannot be attributed to extinction effects since both the depth and the profile of the silicate absorption feature at 9.7 μm remain the same at $z < 1$ and $z \gtrsim 1$. When placing the observed galaxies on IR color-color diagrams, we find that the wedge defining AGN comprises most sources with continuum-dominated spectra, but also contains many starbursts and sources with strong silicate absorption at 9.7 μm . The comparison of the 11.3 μm PAH EW and the *H*-band effective radius, measured from *Hubble* Space Telescope data, indicates that sources with $\text{EWs} \geq 2 \mu\text{m}$, are typically more extended than ~ 3 kpc. However, there is no strong correlation between the MIR spectral type and the near-IR extent of the sources.

Subject headings: infrared: galaxies — ISM: dust, extinction — galaxies: evolution — galaxies: active — galaxies: formation — galaxies: high-redshift — galaxies: starburst — galaxies: interactions

¹Spitzer Science Center, California Institute of Technology, Mail Code 220-6, 1200 East California Blvd, Pasadena, CA 91125

²Infrared Processing and Analysis Center, California Institute of Technology, Mail Code 100-22, Pasadena, CA 91125

³Department of Astronomy, Haverford College, Haverford, PA 19041

⁴Department of Astrophysical Sciences, Princeton University, Princeton, NJ 08544-1001

1. Introduction

Infrared (IR) bright galaxies at intermediate and high redshift, i.e., $0.5 \lesssim z \lesssim 3$, play an important role in driving galaxy evolution since they are in the process of forming new stars (Carilli et al. 2005; Solomon & Van den Bout 2005; Tacconi et al. 2006) or growing black holes (e.g. Alexander et al. 2008, Sajina et al. 2008), and since they are often associated with galactic interactions (Zheng et al. 2004; Dasyra et al.

2008a). The number density of both IR-bright galaxies and galactic interactions evolves strongly with redshift, increasing to at least $z \sim 1$ (Chary & Elbaz 2001; Le Floc'h et al. 2005; Pérez-González et al. 2005; Conselice 2006; Kartaltepe et al. 2007). This cosmologically significant population of galaxies with IR-excess, which often comprises galaxies that are selected in sub-millimeter wavelengths (Valiante et al. 2007; Menéndez-Delmestre et al. 2007; 2009; Pope et al. 2008) or that have extremely red colors in the optical and near-infrared (NIR) wavelengths (Yan et al. 2004b; Daddi et al. 2005; Papovich et al. 2006), is believed to form many of the early-type galaxies (Daddi et al. 2004; Yan et al. 2004a; Swinbank et al. 2006) and possibly some of the late-type galaxies (Hammer et al. 2005) that we observe in the local Universe.

Thousands of new IR-bright galaxies were discovered with the *Spitzer* Space Telescope in the 24 μm catalog of various surveys (Fadda et al. 2004; Papovich et al. 2004; Rigby et al. 2004; Houck et al. 2005; Surace et al. 2005) thanks to the high sensitivity of the Multiband Imaging Photometer for *Spitzer* (MIPS). Many of these systems were spectroscopically followed up with the IR spectrograph (IRS) on board *Spitzer* to determine their redshifts and to reveal the origin of their IR emission. The z determination from mid-infrared (MIR) spectra was very efficient because of the bright and broad polycyclic aromatic hydrocarbon (PAH) features that can be observed within the IRS spectral range, $\sim 5\text{--}35\ \mu\text{m}$, for sources at $z \lesssim 3.5$. This led to the discovery of a large number of galaxies at $1 < z < 3$, complementing previous studies that aimed to populate the so-called 'redshift desert' of optical spectroscopy (Adelberger et al. 2004; Steidel et al. 2004).

The IRS spectra often revealed different powering mechanisms for the MIR emission of these distant IR-bright sources because of the different selection techniques that were applied for each program. Dey et al. (2008) imposed a high 24 μm flux, f_{24} , to R -band flux ratio to select systems more obscured than local ultraluminous IR galaxies (ULIRGs). They detected a large number of sources with continuum-dominated spectra, especially for $f_{24} \gtrsim 1$ mJy (Dey et al. 2009). Other authors used a radio flux cutoff that also led to the identification of several active galac-

tic nuclei (AGN; Martínez-Sansigre et al. 2008; Weedman et al. 2006). Star-forming galaxies, as determined by their PAH emission, were found in samples with different selection criteria. Yan et al. (2005; 2007) identified new $1 < z < 3$ starbursts by imposing that the ratio of their 24 μm flux to their 8 μm flux and the ratio of their 24 μm flux to their R -band flux are as low as those of local starbursts. Farrah et al. (2008), Huang et al. (2009), and Desai et al. (2009) collected IRS spectra for sources with a flux excess in Infrared Array Camera (IRAC) channels that corresponded to the 1.6 μm stellar bump. Their samples comprised a large number of $z \sim 2$ star-forming galaxies. Sub-millimeter galaxies were also followed-up with IRS and were found to be primarily star-forming, but to also have a nonnegligible AGN contribution to their MIR luminosity (Valiante et al. 2007; Menéndez-Delmestre et al. 2007; 2009; Pope et al. 2008). Hernán-Caballero et al. (2009) observed with IRS a sample of $z > 1$ galaxies that have detections in several optical bands. Their sample comprised several composite systems, i.e., systems with weak PAH or silicate absorption feature(s) and an AGN continuum.

The goal of this project is to use a purely flux-limited sample of 150 IR-bright galaxies spanning a wide z range to investigate what are the processes that lead to an excess of IR activity at different epochs. We have been awarded time with *Spitzer* and with the *Hubble* Space Telescope (*HST*) to collect IR imaging and spectroscopic datasets to address what type of galaxies undergo IR-luminous phases at different z . Our program aims to investigate whether there are changes in the interstellar medium properties of these galaxies with look-back time, and whether there is any relation between the dominant MIR emission mechanism and the morphologies of these galaxies. In this paper, we present the catalog of the IRS spectra and we primarily study the behavior of MIR line and feature properties as a function of z .

The rest of this paper is organized as follows. In § 2 we describe the sample selection technique, followed by the presentation of ancillary and complementary datasets for the sample in § 3. The methods that we used to reduce and analyze the spectra are presented in § 4. Results are pre-

sented in § 5, followed by a discussion on MIR spectral properties with z and a summary of our conclusions in § 6 and § 7, respectively. Throughout this paper we use a Λ CDM cosmology with $H_0=70 \text{ km s}^{-1} \text{ Mpc}^{-1}$, $\Omega_m=0.3$, and $\Omega_\Lambda=0.7$.

2. Sample selection

The sample comprises 150 sources that were selected from the 24 μm mosaic of the 3.7 deg 2 *Spitzer* extragalactic first look survey (XFLS; Fadda et al. 2006). It was selected to be flux limited with a lower flux threshold of $\sim 0.9 \text{ mJy}$ at 24 μm . To facilitate the selection of high- z objects, we observed only sources that are fainter than 19 Vega magnitudes in the R band. We also restricted the selection to an area that covers approximately three quarters of the total XFLS field of view and that is located at the center of the field (Fig. 1). An advantage of selecting sources from the central XFLS region is that it comprises a 0.25 deg 2 field with deep IRAC datasets (Lacy et al. 2005), the so-called ‘verification zone’. Moreover, IRS spectra have also been acquired for several sources with $f_{24} \gtrsim 0.9 \text{ mJy}$ in the same region as part of other programs (PIs Borys, Fazio, Lacy, Lagache, Martinez-Sansigre, Weedman, Yan). These archival data can be merged with data from our program, with ID 20629, to create an extended sample that is highly complete at faint optical magnitudes and that will be used for luminosity function studies (Yan et al. 2009, in preparation).

In total, new IRS observations were executed for 150 XFLS sources as part of the program with ID 20629. This led to the acquisition of MIR spectra for one out of every three extragalactic sources in the central XFLS field with $f_{24} \geq 0.9 \text{ mJy}$ and $m_R \geq 20$ Vega mags (Fig. 2). Similarly, this sample is 57% complete for $m_R \geq 22$ Vega magnitudes within the selected area (Fig. 2). The datasets were collected during the second *Spitzer* cycle. The coordinates of the observed sources and their integration times per mode are presented in Table 1. The total integration time per target varied from 25 mins to 2 hours on-source. The integration times were longer at wavelengths $\gtrsim 14 \mu\text{m}$ than at wavelengths $\lesssim 14 \mu\text{m}$ to compensate for the lower sensitivity of the instrument at long wavelengths.

3. Ancillary data collection and reduction

The XFLS region has a plethora of ancillary datasets. Fadda et al. (2004) presented an R -band mosaic with a corresponding catalog that has a depth of 25.5 Vega magnitudes. Imaging datasets for all IRAC channels, at 3.6, 4.5, 5.8, and 8.0 μm , are available in the Lacy et al. (2005) catalogs. Each IRAC flux is measured within a fixed aperture of either 6''.0, 9''.3, 14''.9, or 24''.4 that is optimally determined for each galaxy and band (Lacy et al. 2005). When possible, we used the deep ‘verification-zone’ IRAC data. The ancillary datasets that we compiled, together with the MIPS 24 μm fluxes of the sources (Fadda et al. 2006) are presented in Table 1.

To enhance the accuracy of the analysis presented in this paper, we examined the proper identification of the counterpart of each 24 μm source in all IRAC channels. We remeasured IRAC fluxes or limits for 15% of the galaxies because of counterpart misidentification or overlap of nearby sources. We deblended IRAC overlapping sources when one of them was a star or a galaxy that did not contribute to the MIPS 24 μm flux. We also deblended overlapping sources when the 24 μm emission peaked near one of the sources, unless their *HST* image showed clear evidence of interactions between them. Vice versa, we typically merged the fluxes of two IRAC detections within the 24 μm beam if the 24 μm flux peaked between them. Moreover, all IRAC limits were remeasured, since Lacy et al. (2005) used statistical completeness limits for their catalogs.

To perform aperture photometry, we used the SExtractor package (Bertin & Arnouts 1996) with the same parameters as those used by Lacy et al. (2005), except for the background and the minimum deblending parameter. We computed the background locally (within 1 square arc minute) and we set the deblending parameter to 0.001, to easily deblend overlapping sources. We used the optimal extraction aperture of each source, as chosen by Lacy et al. (2005), with the corresponding aperture flux correction for the specific channel. To measure the flux limit of a source that is undetected at a given channel, we used its aperture at the nearest channel(s) in which the source was detected. If two such apertures existed, we chose the largest of the two. To deblend over-

lapping sources, we decomposed them into two or more point sources using the package GALFIT (Peng et al. 2002). After determining the intensity of each individual point-spread-function (PSF), we subtracted all PSF models that were unrelated to the $24\text{ }\mu\text{m}$ source. We then measured the flux of the deblended counterpart of the $24\text{ }\mu\text{m}$ source using SExtractor (with the same parameters as above), to avoid systematic effects in our measurements.

A cleaning analysis similar to that performed for the IRAC catalogs was also performed for the R -band catalog fluxes of Fadda et al. (2006). We remeasured the R -band fluxes for sources that were erroneously identified as the counterpart of the $24\text{ }\mu\text{m}$ source. Whenever we merged the IRAC fluxes of two overlapping sources, we also merged their R -band fluxes. To measure R -band fluxes, we used SExtractor with the zeropoints of the original catalog. We kept most parameters identical to those selected by Fadda et al. (2006), including the automatic determination of the optimal aperture. We set the area that is used to compute the background flux to 1 square arc minute. We used deblending parameter values in the range [0.1,0.001] to ensure the proper deblending of nearby sources. In Table 1, we summarize all remeasured IRAC and R -band fluxes or limits.

Shallow MIPS 70 and $160\text{ }\mu\text{m}$ catalogs are also available for the XFLS (Frayer et al. 2006). We were awarded time to complement the $70\text{ }\mu\text{m}$ catalog with deeper MIPS observations for two thirds of the sources in our sample. The MIPS datasets will be presented in Sajina et al. (2009, in preparation), together a multi-wavelength spectral energy distribution (SED) fitting that aims on the computation of the bolometric luminosities of the sources.

As part of the same large, joint *Spitzer* and *HST* program, we also acquired *HST* H -band images of several sources with the Near Infrared Camera and Multi-Object Spectrometer (NICMOS). In total, NICMOS successfully observed 102 sources. We processed the NICMOS images similar to those in Dasyra et al. (2008a), and we used them to measure effective radii R_{eff} using SExtractor (Table 1; Zamojski et al. 2009, in preparation). The NICMOS data and their reduction techniques will be presented in detail in Zamojski et al. (2009, in preparation).

4. IRS data reduction and analysis

4.1. Data reduction procedures

The IRS data reduction began with the processing of the basic calibration datasets (BCDs) by the IRS pipeline version 15.3. The pipeline converts the up-the-ramp exposures to a single image and then performs dark subtraction, linearity correction, flat division and other instrument-related corrections to the image. Details on the pipeline products can be found at the IRS data and pipeline handbooks that are available at the *Spitzer* Science Center (SSC) webpage¹. The pipeline provides the two-dimensional spectral images together with their uncertainties and mask files for each of nod position and wavelength range.

There are two wavelength ranges for the low-resolution mode of the IRS spectrograph: the short-low (SL) and long-low (LL) modes that can obtain datasets in the wavelength ranges [5.2,14.7] μm and [14.3,35.0] μm , respectively. For LL data, we removed the sky background for each order and nod position using IDL routines that compute the median sky image for all other orders and nod positions of the same source. Because in SL we only obtained order 1 data, we simply subtracted one nod position from the other to remove the sky background. The sky subtraction was performed with the code used by Yan et al. (2005). We then performed an automated first-order rejection of negative bad pixels, and an inspection and manual removal (when necessary) of positive bad pixels that deviated by more than 3 standard deviations σ from the median value of the spectrum. The manual rejection of bad pixels was performed using the IDL routine IRSCLEAN² provided by the SSC. The values of bad pixels were interpolated from those of their neighbors. We extracted the spectrum of each nod position using the SSC package SPICE³. For the extraction of the spectrum, we used the 'optimal' technique, which is recommended for faint source spectroscopy. This technique maximizes the signal-to-noise ratio of the spectrum by weighting the spatial pixels at any wavelength prior adding them. The code uses the

¹ <http://ssc.spitzer.caltech.edu/irs/dh/dh32.pdf> and <http://ssc.spitzer.caltech.edu/irs/dh/irsPDDmar30.pdf>

² <http://ssc.spitzer.caltech.edu/postbcd/irsclean.html>

³ <http://ssc.spitzer.caltech.edu/postbcd/spice.html>

spatial profile of a point source to compute the appropriate weights. The extracted one-dimensional spectrum and its uncertainty image are then flux calibrated. Aperture-loss and slit-loss corrections are applied based on a point-source profile. After extracting the spectrum for both nod positions of each spectral order, we computed the average spectrum for both nod positions and trimmed all (noisy) edges. We merged the final spectra and interpolated the flux values in the wavelength range where different orders overlap to the wavelength values of the order with the lower spectral resolution.

4.2. Analysis techniques

To compute the redshift of each source we first ran a code that simultaneously fits MIR fine-structure lines and PAHs using Gaussian and Lorentzian functions, respectively, using an initial redshift guess. After fitting the spectrum, the code returns the best z solution by averaging the redshift of all 3σ detected lines and features that are within $0.2 \mu\text{m}$ from their expected wavelength. In Table 2, we summarize the confidence and errors of all measured z values. We define the z measurement of a source reliable when its spectrum has more than two 3σ detected emission lines or features, or silicate absorption at $9.7 \mu\text{m}$, or a combination of the two (see source confidence classifications a , b , and c in Table 2). All sources with uncertain redshift measurement, e.g., because more than one redshift solutions are plausible, are excluded from the analysis in this paper. The fully reduced spectra are presented in the rest frame for the 95 sources with reliable z measurement (Fig. 3), and in the observed frame for the 55 sources with unknown or uncertain redshift (Fig. 4).

For sources with reliably measured redshift, we ran the fitting algorithm PAHFIT (Smith et al. 2007) to derive the fluxes of lines and features and the optical depth τ of the obscuring medium in the MIR. PAHFIT decomposes MIR spectra into emission originating from ionic and molecular lines, PAH features, dust continuum and stellar continuum. All components are multiplied with an extinction curve prior to being added. The best-fit solution of the observed spectrum is computed using a χ^2 minimization method. The code returns the best-fit parameters for each of the components,

including the line or feature fluxes and the optical depth of the silicate absorption feature at $9.7 \mu\text{m}$, $\tau_{9.7}$.

The rest-frame spectrum of each source was used as input to PAHFIT. The spectral flux per frequency was divided by a factor of $(1+z)$ so that all line fluxes are correctly measured at rest frame, where PAHFIT performs all line flux computations. We added all available IRAC datapoints to the spectra, so that PAHFIT can best constrain the stellar continuum emission. Since the default PAHFIT parameters were optimized to fit local low-luminosity sources, we modified several parameters to make the code appropriate for high- z IR-bright galaxies. To include a rising AGN continuum for $\lambda \lesssim 10 \mu\text{m}$, we allowed the dust grains to have temperatures of 400, 600, 800, 1000, 1200, or 1400K, which are higher than the default temperatures that PAHFIT uses ($\leq 300\text{K}$). By default, PAHFIT returns extinction-corrected line fluxes. Because the geometric distribution of dust grains in high- z obscured galaxies is not known, we measured and used throughout this paper fluxes that are not extinction corrected. For this reason, we run PAHFIT assuming a screen Galactic center extinction (Chiar & Tielens 2006), and we then multiplied the measured fluxes with the extinction curve value at the center of each line or PAH complex. The PAHFIT best-fit solution for each spectrum is presented in Fig. 3.

To measure line or feature equivalent widths (EWs), we divided the best-fit profile of each individual line or feature, which has no continuum, by the combined continuum of dust and stars. We then integrated the result as a function of wavelength. Fluxes (or 3σ flux limits) and EWs of the most common bright lines and features in the IRS spectra are summarized in Tables 3 and 4. Fluxes of lines or features whose continuum cannot be well determined are not tabulated. For example, we do not present an $8.6 \mu\text{m}$ PAH flux measurement when silicate absorption is present and the continuum shortward of the $7.7 \mu\text{m}$ PAH is outside the spectral range.

We note that variations can exist between the fluxes and the signal-to-noise ratios of features that are detected with the simple fitting algorithm that we used to derive redshifts (Table 2) and those of features that are detected with PAHFIT (Tables 3 and 4) because of different con-

tinuum assumptions. To get an estimate of the deviations in the fluxes provided by various codes, we also ran the fitting algorithm of Sajina et al. (2007) for all spectra with well-determined redshifts. While we found no significant differences for fluxes of PAHs at $\lambda > 10 \mu\text{m}$, systematic differences were observed for the short-wavelength features. The fluxes of both the 6.2 and the 7.7 μm PAHs, when derived with PAHFIT, are on average 1.5 times higher than those measured with the code of Sajina et al. (2007). The discrepancies are high for the 7.7 μm PAH because it is located at the edges of the 9.7 μm absorption feature and because it is partially blended with the 8.6 μm PAH. The statistics are poor for the 6.2 μm PAH because it is either undetected or outside the spectral range in many sources. Because we would like to use diagnostics that depend little on the choice of model (continuum) parameters and that are applicable to the majority of the sources in this sample, we used the EW of the 11.3 μm feature, $\text{EW}_{11.3}$, to define sources with MIR spectra resembling those of AGN or starbursts (see also Desai et al. 2007). Despite that the 11.3 μm feature can be heavily obscured, the $\text{EW}_{11.3}$ measurements presented in this paper are independent of the selected extinction law because the continuum and the PAHs are equally obscured for a screen geometry. Different geometric distributions of the obscuring medium could affect $\text{EW}_{11.3}$. Still, we opt to use it to distinguish the MIR spectral type of the sources because otherwise we would be restricted in using the EW of the 12.7 μm PAH. This would render our classification highly uncertain because the 12.7 μm PAH is blended with the [Ne II] line at 12.81 μm .

To determine the $\text{EW}_{11.3}$ thresholds that we used to define AGN and starbursts, we ran PAHFIT for the local templates presented in Armus et al. (2007). We used the same PAHFIT parameters for the local templates as for the sources in our sample. Based on this calibration, we chose to classify as star-forming galaxies those with $\text{EW}_{11.3} > 0.8 \mu\text{m}$. This threshold selects sources with star-formation contribution to their MIR luminosity that is likely to exceed $\sim 90\%$, as in NGC 6240, IRAS 12112+0305, and IRAS 14348-1447. Similarly, we define as AGN the sources with $\text{EW}_{11.3} \leq 0.1 \mu\text{m}$, since this cutoff comprises sources with AGN contribution to their

MIR luminosity that is likely to exceed $\sim 90\%$, as in IRAS 05189-2524, IRAS08572+3915, Mrk 231, Mrk 463, and Mrk 1014 (Armus et al. 2007).

5. Results

5.1. Redshift distribution and estimated IR luminosities of the sources

Using redshifts derived from the IRS spectra, we find that the redshift distribution of the sources in this sample peaks at $z=1$, with average and median z values of 1.12 and 0.96, respectively. The z range that this sample spans is fairly high, with the lowest z and the highest z source being at $z=0.3$ and $z=3.5$, respectively (Fig. 5).

To obtain an estimate of each source's bolometric IR luminosity, L_{IR} , we used the 14 μm continuum luminosity, which is available for most sources and which is little affected by PAH emission. We used the relation between L_{14} and L_{IR} presented in Sajina et al. (2008) because of the similarities in the IRS spectra of the two IR-bright galaxy populations. We find that most sources at $z \gtrsim 1$ are ULIRGs, with $L_{\text{IR}} \geq 10^{12} L_{\odot}$. Most sources at $z < 1$ are luminous infrared galaxies (LIRGs), with $10^{11} \leq L_{\text{IR}} < 10^{12} L_{\odot}$ (Fig. 6). Because of the scatter in the relation that we used, the computation of L_{IR} from L_{14} can be uncertain by a factor of at least 2.

5.2. Detection of weak lines through spectral stacking

To investigate for weak lines that are hard to detect in individual spectra of high- z galaxies, we performed a stacking analysis using sources with well determined redshifts. We began the stacking procedure by dividing the flux (per frequency) of each source by a factor of $(1+z)$ in order to correctly measure line fluxes at the rest frame. We determined the continuum of each source by fitting a spline function at feature-free wavelengths and subtracted it, so that the weak features that we are trying to detect are not diluted into the continuum of the brightest galaxies. Moreover, adding spectra with different MIR continuum slopes could create artificial bumps in the resulting spectrum at the wavelengths where the individual spectra start or end. We then stacked the continuum-subtracted spectra by computing their weighted average using their uncertainty images as weights.

To enhance the probability of detecting weak lines, we stacked sources that already have line detections. For this reason, we used the spectra of all sources with [Ne II] emission, which originates from an ion that is found both in star-forming regions and in AGN.

The resulting stacked spectrum is presented in Fig. 7. It contains molecular lines, i.e., the H₂ 0-0 S(1) and S(3) lines, detected with fluxes of $2.65 (\pm 0.30) \times 10^{-23}$ W cm⁻² and $2.42 (\pm 0.41) \times 10^{-23}$ W cm⁻², respectively. It is unclear whether the line at 6.9 μm originates from the H₂ 0-0 S(5) transition, since the H₂ line could be blended with [Ar II] at 6.99 μm . Assuming that the stacked spectrum is at $z=0.85$, which is the average redshift of the individual spectra used for its construction, we find that the S(1) and S(3) line luminosities are $2.42 (\pm 0.27) \times 10^8 L_\odot$ and $2.21 (\pm 0.37) \times 10^8 L_\odot$, respectively. Using the median L_{IR} value of the sources that were used for the computation of the stacked spectrum, $2.2 \times 10^{12} L_\odot$, we find that the ratio of the S(1) and S(3) line luminosities to L_{IR} is of order 10^{-4} , as in several local ULIRGs (Higdon et al. 2006). We computed the excitation temperature and the mass of the warm molecular hydrogen using the S(1) and S(3) line luminosities and the technique and assumptions of Higdon et al. (2006). We find that the H₂ gas has an excitation temperature of 360 (± 5) K and a mass of $2.06 (\pm 0.26) \times 10^8 M_\odot$, similar to those in local IR-bright galaxies (Rigopoulou et al. 2002; Higdon et al. 2006).

Spectral stacking also leads to the detection of a line at 14.32 μm (Fig. 7), which corresponds to [Ne V] and which is frequently found in AGN. [Ne V] can be blended with [Cl II] at 14.37 μm , which is primarily found in spectra of star-forming galaxies because Cl II only needs 23.81 eV to be ionized to Cl III. To test whether this line primarily originates from Ne V or Cl II ions, we ran our stacking algorithm in a manner than can allow us to investigate how the stacked spectrum changes for different AGN and star-formation luminosities. For this reason, we stacked sources with different 11.3 μm PAH strength (Fig. 8). We find that the flux of the line increases with decreasing EW_{11.3} (or with increasing AGN contribution to the MIR luminosity). Specifically, the line flux increases from 4.02×10^{-23} W cm⁻² for sources with EW_{11.3} < 0.5 μm to 9.29×10^{-23} W cm⁻² for

sources with EW_{11.3} < 0.1 μm . This indicates that a significant fraction of the flux originates from an ion of high ionization potential, i.e., [Ne V]. Since the ionization potential of [Ne V] is 97.12 eV, its detection provides direct evidence for the presence of an AGN in some of the sources in this sample (Dasyra et al. 2008b).

We also investigated whether we can detect the PAH feature at 3.3 μm that has been seen in several local galaxies (Sturm et al. 2000; Imanishi 2002; Imanishi et al. 2006; Risaliti et al. 2006). The PAH feature was detected at $\sim 5\sigma$ levels in the stacked spectrum of sources with [Ne II] detections (Fig. 7) with a flux of 3.37×10^{-22} W cm⁻². Since the flux of the 6.2 μm PAH is 7.50×10^{-22} W cm⁻², the flux ratio of the 6.2 μm PAH to the 3.3 μm PAH is 2.22, which is plausible for PAHs that are mainly neutral (Draine & Li 2007). Using $z=0.85$ and $L_{\text{IR}}=2.2 \times 10^{12} L_\odot$ for the stacked spectrum, we find that the 3.3 μm feature luminosity, $L_{3.3}$, is $3.07 \times 10^9 L_\odot$ or $\sim 0.001 \times L_{\text{IR}}$. The 6.2 μm feature luminosity, $L_{6.2}$, is $6.84 \times 10^9 L_\odot$. The ratio $L_{6.2}/L_{\text{IR}}$ is ~ 0.003 , which is typical for local starbursts (Peeters et al. 2004). The 3.3 μm feature has also been detected with comparable $L_{3.3}/L_{\text{IR}}$ and $L_{6.2}/L_{3.3}$ ratios in an XFLS source with deep IRS spectra (Sajina et al. 2009, in preparation). Still, the $L_{3.3}/L_{\text{IR}}$ ratio is a factor of 3 higher than the highest $L_{3.3}/L_{\text{IR}}$ ratio found in a local ULIRG (Imanishi et al. 2006; 2008). This difference could be due to uncertainties in the determination of L_{IR} or due to changes in the relative PAH strengths with z (see § 6).

5.3. AGN vs star-formation properties

Using the EW_{11.3} threshold of 0.8 μm , we determined that the number of sources that have MIR spectra resembling those of starbursts is 39 (or 26%). Similarly, the number of sources that are continuum-dominated is 49 (or 33%). Of these 49 sources, 31 have featureless MIR spectra and no z measurement.

The AGN contribution to the MIR luminosity of the sources increases with z . This can be demonstrated by the decreasing EW of PAHs with z (Fig 9). Moreover, the [Ne III]/[Ne II] flux ratio increases with z , indicating that the radiation field in the most distant sources is harder than that in the most nearby sources (Fig. 10). This effect is also seen as a function of luminosity possibly due

to the flux-limited selection of the sample.

In Fig. 11, we constructed a diagnostic diagram between the [Ne III]/[Ne II] flux ratio and $\text{EW}_{11.3}$, which determines the powering mechanism of a source's MIR emission. While this diagram does not use lines with large difference in ionic excitation potential (e.g., Genzel et al. 1998, Peeters et al. 2004, Dale et al. 2006, Armus et al. 2007) or two different states of the same ion (e.g., Sturm et al. 2002; Verma et al. 2003; Farrah et al. 2007), it is useful because it uses lines in the range $11 < \lambda < 16 \mu\text{m}$. Hence, it can be applied to samples that span a wide z range, i.e., $0 \leq z \leq 1.3$ for samples observed with IRS. We used the local templates Mrk 1014 and IRAS 12112+0305 to demonstrate how the position of a source on this diagram changes when the AGN (or star-formation) fraction of L_{14} increases from 0 to 100%. We also plotted the positions of several local templates to investigate for differences between distant IR-bright galaxies and their local analogues. Because ionic lines are hard to detect in distant AGN, most of the sources in our sample that are used to populate this diagram are either composite or starburst dominated, i.e., they have $\text{EW}_{11.3} > 0.1$ and $> 0.8 \mu\text{m}$, respectively. We find that, at intermediate and high z , IR-bright galaxies often have a radiation field that is harder than that in their local analogues, with ULIRGs being more AGN dominated than LIRGs. Based on their locus on this diagram, several distant star-forming galaxies could resemble NGC 6240, which has a buried active nucleus (Komossa et al. 2003; Armus et al. 2006; Farrah et al. 2007). Buried AGN have been discovered in X-ray data of $z \sim 2$ starbursts (Huang et al. 2009). Moreover, the $\text{EW}_{11.3}$ values of many distant starbursts are higher than those of local ULIRGs, indicating a possible increase in star formation activity with z (Weedman & Houck 2008). The few heavily obscured sources in the MIR that are seen on this diagram may be hosting an AGN. However, the dominant mechanism of their MIR emission is unclear.

5.4. IR color-color diagrams vs MIR spectral type

Color-color diagrams in the IR (Lacy et al. 2004; Stern et al. 2005) have provided a way to select AGN, allowing IR samples to largely

complement X -ray samples in the identification of type-2 QSOs (Barmby et al. 2006; Pogosyan et al. 2006, 2007; Donley et al. 2007; Georgantopoulos et al. 2007; Lacy et al. 2007; Barger et al. 2008; Cardamone et al. 2008; Gorjian et al. 2008). These diagrams use 3.6–8.0 μm broadband photometry to determine whether the NIR–MIR SED of extragalactic sources resemble those of AGN.

Using the updated IRAC fluxes of the sources in this sample (Table 1) and the AGN and star-forming galaxy classification based on $\text{EW}_{11.3}$, we investigated how well the MIR spectral type classification agrees with the color-color diagram classification. For this purpose, we constructed the Lacy et al. (2004) and Stern et al. (2005) diagrams for the 141 sources with detections in all four IRAC channels (Fig. 12). We displayed on these diagrams sources with AGN and star-formation dominated spectra, and sources that are highly obscured in the MIR (with $\tau_{9.7} \geq 1$). Sources without z have featureless MIR continua and are therefore also classified as AGN. We find that the number of sources that lie inside the AGN wedge, which is the area enclosed by the dashed lines, was 122 (or 87%) for the Lacy et al. (2004) diagram and 88 (or 62%) for the Stern et al. (2005) diagram. In most cases, spectroscopically determined AGN with or without z lie inside the AGN wedge. However, some star-forming galaxies and many heavily obscured systems are also located inside the same wedge. A plausible explanation why this diagram could lead to the misidentification of starbursts as AGN is z effects. The use of rest-frame IRAC fluxes can bring sources outside the AGN wedge boundaries or close to them (Barmby et al. 2006; Donley et al. 2007; Higdon et al. 2008; Yun et al. 2008).

5.5. MIR spectral properties vs NIR radial extent

Previous NIR imaging of distant 24 μm selected sources indicated that $z \sim 2$ ULIRGs with large radial extents typically have MIR spectra resembling those of star-forming galaxies. Sources with continuum-dominated MIR spectra are often compact, while the extent of systems with high MIR obscuration can vary (Dasyra et al. 2008a; Melbourne et al. 2009). Using this large sample, we populated the redshift range $0 \lesssim z \lesssim 2$ to investi-

gate whether this trend is typical of IR-luminous galaxies at several epochs.

We confirm that composite sources and sources that are heavily obscured in the MIR (i.e., sources with $\tau_{9.7} \geq 1$) can either have a compact or an extended stellar distribution (Fig. 13). One of the heavily obscured sources in the MIR, MIPS 562, is one of the most extended sources in the *HST* images with two (or possibly more) closely interacting gas-rich components. We also find that the sources with the strongest $\text{EW}_{11.3}$ values, i.e., $\text{EW}_{11.3} \geq 2 \mu\text{m}$, are typically more extended than $\sim 3 \text{ kpc}$ (Fig. 13). However, there is no strong correlation between $\text{EW}_{11.3}$ and the observed-frame NIR radial extent of the sources.

Scenarios of local gas-rich galaxy mergers suggest that the IR SED becomes warmer (Sanders et al. 1988), the IR luminosity increases (Veilleux et al. 2006), and the $\text{EW}_{11.3}$ value decreases (Farrah et al. 2009) as a merger advances, approaching dynamical equilibrium. In such scenarios, the radial extent of interacting galaxies would correlate with $\text{EW}_{11.3}$. The lack of a strong correlation could be due to the large scatter in the merger timescales during which the peak of star-formation (or AGN) activity is observed (Rigopoulou et al. 1999). Moreover, several of the distant IR-bright galaxies may not be associated with interactions (Zheng et al. 2004; Dasyra et al. 2008a).

6. Discussion: Changes in the MIR spectral properties with z or L

Having a flux-limited sample of IR-luminous galaxies spanning a wide z range, we investigated for differences in the properties of spectral features with look-back time by comparing the stacked spectra of sources in different z bins. To create a representative spectrum for each z bin, we used a stacking algorithm that was similar to that presented in § 5.2. We first divided each spectrum by its extinction curve so that the line ratios in the stacked spectrum are not affected by differences in the silicate depth among individual galaxies. For each extinction-corrected spectrum, we then subtracted the continuum and divided the flux at all wavelengths by its $11.3 \mu\text{m}$ value, so that all sources have similar $11.3 \mu\text{m}$ PAH strength. The resulting stacked spectrum, which was computed using all galaxy spectra with

rest-frame $11.3 \mu\text{m}$ data, was found by averaging the individual spectra using their uncertainties as weights. It is shown in Fig. 14 for sources at $z \geq 1$ and $z < 1$. We observe a small but significant ($>3\sigma$) change in the fluxes of several PAH features with z . For example, the normalized flux of the $7.7 \mu\text{m}$ PAH is 22% higher at $z \geq 1$ than at $z < 1$. Such flux variations are frequently seen within local galaxies (Galliano et al. 2008). The ratio of the $11.3 \mu\text{m}$ PAH flux, $f_{11.3}$, to the flux of the PAHs at $7.7 \mu\text{m}$ and $8.6 \mu\text{m}$ decreases with increasing redshift. Changes in the PAH radius or excitation state can reproduce this trend. For example, an increasing fraction of ionized PAHs leads to stronger PAH emission at $6-9 \mu\text{m}$ than at $11.3 \mu\text{m}$ (Draine & Lee 1984; Allamandola et al. 1999; Draine & Li 2007; Farrah et al. 2008).

To investigate whether some of the observed trends could be attributed to a change in the extinction curve shape with z , we computed the stacked spectrum of the $9.7 \mu\text{m}$ absorption profile at $z < 1$ and $z \geq 1$. For this reason, we removed both the continuum and the best-fit profile of all lines and features in each individual spectrum. We normalized all spectra at $9.7 \mu\text{m}$, and computed the average spectrum using only sources with intermediate and high extinction, i.e. $\tau_{9.7} \geq 0.5$. We also used only sources with $\text{EW}_{11.3} < 0.8 \mu\text{m}$, so that possible residuals from the removal of lines and features do not affect the absorption feature profile. We find no significant change in the shape of the extinction at $z \geq 1$ and $z < 1$ (Fig. 15). Moreover, there is no correlation between z and the depth of the silicate absorption feature, as computed by PAHFIT (see Table 2), indicating that any changes in the spectral properties with z are primarily due to differences in the PAH properties.

What remains to be tested is whether the observed changes in the spectra of IR-bright galaxies are purely dependent on redshift. Because of the flux-limited nature of the sample, the sources become brighter with increasing z . When computing the stacked spectra of sources as a function of luminosity, we also find that the flux ratio of the $11.3 \mu\text{m}$ PAH over the 7.7 or the $8.6 \mu\text{m}$ complex decreases with the transition from LIRGs to ULIRGs (Fig. 14; see also Farrah et al. 2008). The use of further datasets that extend the sample's L_{IR} range in each z bin will help us break this degeneracy by enabling us to compare the spectra of

LIRGs and ULIRGs at $z \geq 1$ and $z < 1$. For this purpose, we will need to use sources from flux-limited samples of different f_{24} thresholds. Including such samples will also help us to avoid possible biases associated with a single flux threshold, and possibly, cosmic variance. This will be the focus of a forthcoming paper.

7. Conclusions

We presented a MIR spectroscopic catalog of 150 IR-luminous galaxies in the *Spitzer* extragalactic first look survey. Our program aimed to collect data with the IRS spectrograph on board *Spitzer* for a purely flux-limited sample (with $f_{24} \gtrsim 0.9$ mJy and $m_R > 19$ Vega mags) of IR-luminous galaxies in order to investigate for possible evolution in their MIR spectral properties with z . This catalog is complemented by a large number of ancillary datasets, including ground-based R -band images, *HST* H -band imaging, *Spitzer* IRAC (3.6, 4.5, 5.0, and 8.0 μm) and MIPS (24 and 70 μm) photometry. Our basic findings are summarized as follows.

1. Of the 150 observed sources, 31 have featureless MIR continua and 24 have potential but uncertain z measurements. Reliable spectroscopic redshifts were derived for the remaining 95 sources from MIR features. These 95 sources span a wide z range, $0.3 \leq z \leq 3.5$, with a peak at $z=1$. Most of these sources are estimated to be LIRGs at $z < 1$ and ULIRGs at $z \gtrsim 1$, based on their monochromatic 14 μm luminosities.
2. We used the EW of the 11.3 μm PAH to classify sources as AGN dominated ($\text{EW}_{11.3} \leq 0.1 \mu\text{m}$) or star forming ($\text{EW}_{11.3} > 0.8 \mu\text{m}$). We found that the sample comprises 39 star-forming galaxies, 9 of which are simultaneously highly obscured systems (with 9.7 μm optical depth that exceeds unity). The sample also comprises 13 more highly obscured systems with $\text{EW}_{11.3} \leq 0.8 \mu\text{m}$. The galaxies with an AGN-related power-law continuum are 49, including the 31 sources that have no z measurement.
3. The AGN continuum emission becomes stronger with increasing z , as indicated by the decreasing EW of PAH features. Moreover, the interstellar radiation field becomes harder with increasing z , as determined by the increasing $[\text{Ne III}]/[\text{Ne II}]$ flux ratio. These results could be attributed to the flux-limited nature of the sample, since it comprises more luminous, and possibly more AGN-dominated systems, at earlier epochs. Distant ULIRGs are more AGN-dominated than distant LIRGs based on a $[\text{Ne III}]/[\text{Ne II}]$ versus $\text{EW}_{11.3}$ diagram that is used as a diagnostic between AGN and star formation activity. Based on their high $\text{EW}_{11.3}$ values, several distant starbursts can have an elevated star formation activity with respect to their local analogues.
4. We tested how well the power source of the MIR emission, i.e., an AGN or a starburst, as inferred from the IRS spectra, agrees with the position of sources on 3.6–8 μm color-color diagrams. While continuum-dominated sources fall inside the AGN wedge of color-color diagrams, so do some starbursts possibly due to redshift effects. Since most of the heavily obscured sources (with $\tau_{9.7} \geq 1$) also fall inside the AGN wedge, they would be selected as type-2 AGN, even if they were undergoing nuclear starbursts.
5. Stacking analysis enabled the detection of weak features that are often undetected in high- z sources. Such an example is the 14.32 μm $[\text{Ne V}]$ line, which constitutes direct evidence for the existence of an AGN because it is emitted by an ion with high ionization potential. The $[\text{Ne V}]$ line was detected in stacked spectra of sources with low $\text{EW}_{11.3}$, and its flux increased as the $\text{EW}_{11.3}$ decreased. The H_2 0-0 S(1) and S(3) lines were observed in stacked spectra of sources with $[\text{Ne II}]$ emission, which comprised starburst galaxies. The excitation temperature of the warm molecular hydrogen is 360 K and its mass is $2 \times 10^8 M_\odot$. The luminosities of the S(1) and S(3) lines were $\sim 10^{-4} \times L_{\text{IR}}$. The 3.3 μm PAH feature was also detected in the stacked spectra of sources with $[\text{Ne II}]$ emission. Its luminosity was of order $10^{-3} \times L_{\text{IR}}$ and ~ 2 times lower than the luminosity of the 6.2 μm PAH feature.
6. A small (but significant) change in the ratios of PAH features is observed in the stacked

spectra of IR-luminous galaxies with z . The $11.3 \mu\text{m}$ feature flux decreases with respect to the fluxes of the 7.7 and $8.6 \mu\text{m}$ complexes from $z < 1$ to $z \geq 1$, while there is no evidence for change in the profile or the depth of the extinction curve with redshift. The same trend is seen as a function of luminosity. It is possible that this effect is due to changes in the PAH excitation properties.

7. We investigated whether the MIR spectra of IR-luminous galaxies are related to their radial extents in the NIR. While we found no strong correlation between $\text{EW}_{11.3}$ and R_{eff} , as measured from *HST NICMOS H-band* images, the strongest starbursts, i.e., the sources with $\text{EW}_{11.3} > 2 \mu\text{m}$ typically have $R_{\text{eff}} \gtrsim 3 \text{ kpc}$. The extent of sources with composite MIR spectra or with high MIR obscuration can vary.

This work was based on observations made with the *Spitzer* Space Telescope, which is operated by JPL/Caltech under a contract with NASA, and on observations made with the NASA/ESA *Hubble* Space Telescope, obtained at the Space Telescope Science Institute, which is operated by the Association of Universities for Research in Astronomy, Incorporated, under NASA contract NAS5-26555. The observations are associated with the *Spitzer* programs 20629 and 40025, and the *HST* program 11142. The authors acknowledge support by NASA through awards issued by JPL/Caltech and through the grant HST-GO-11142.06-A awarded by the Space Telescope Science Institute.

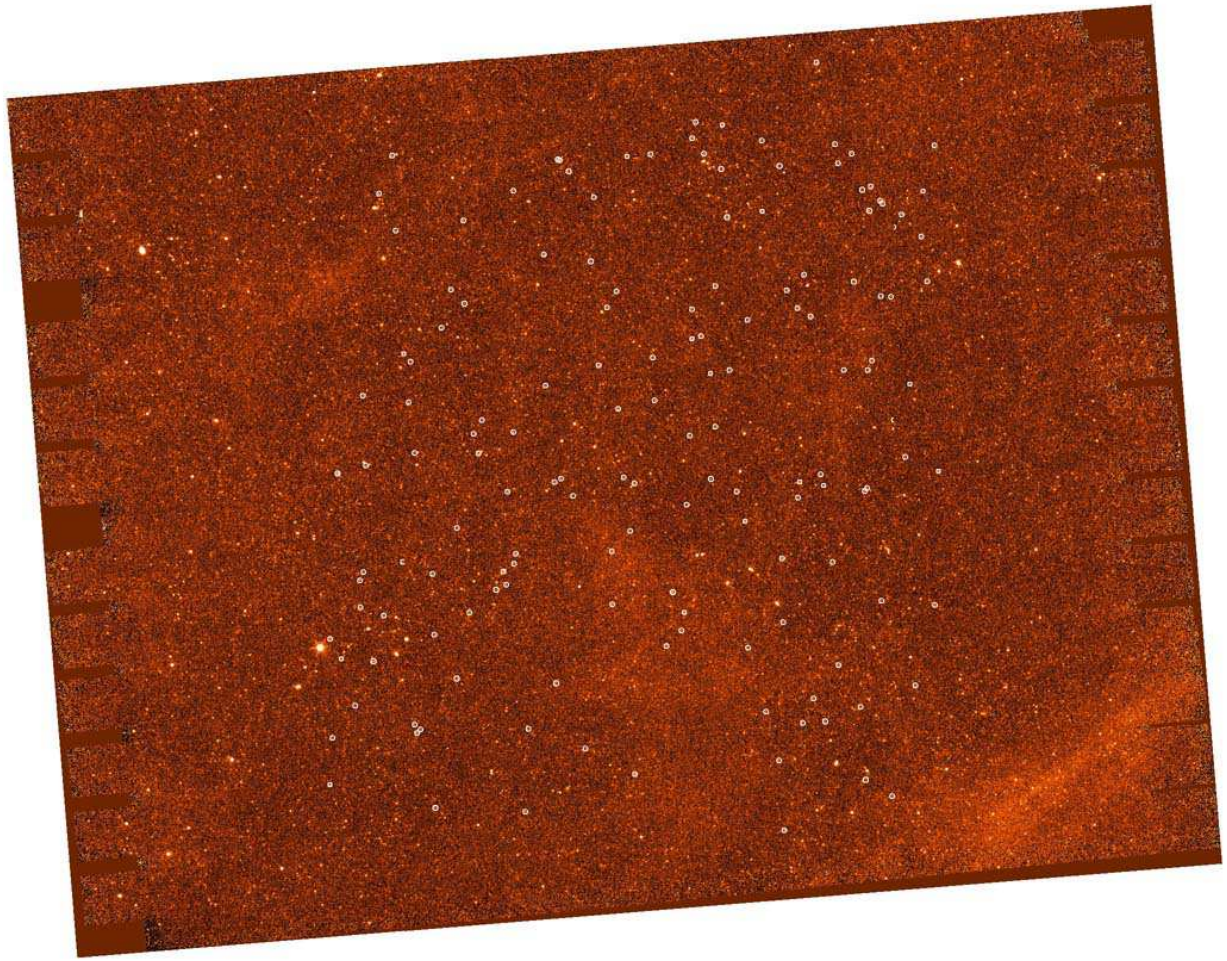


Fig. 1.— Mosaic of the *Spitzer* extragalactic first look survey at $24 \mu\text{m}$ (Fadda et al. 2006). The sources observed with IRS as part of the program with ID 20629 are shown as circles.

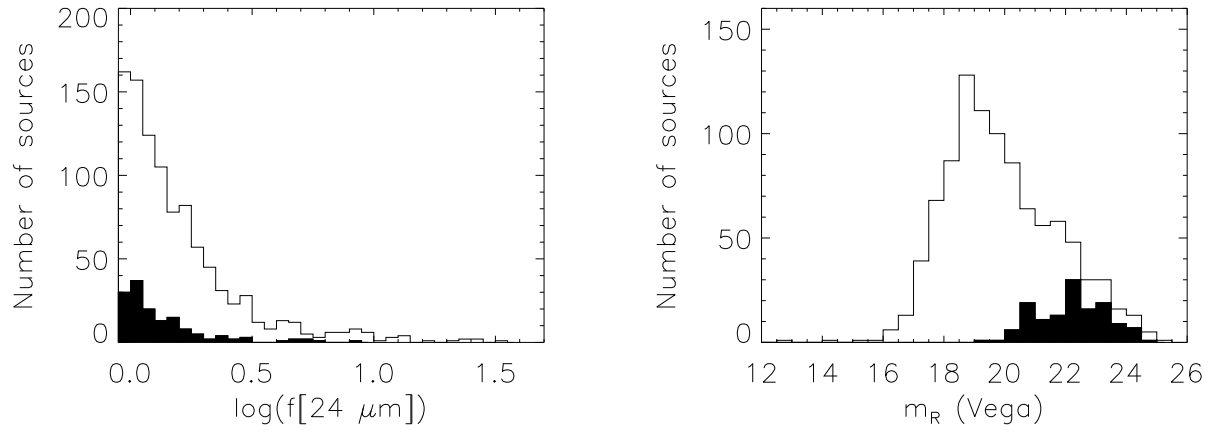


Fig. 2.— Selection function of the sources in this sample. The histogram of the logarithm of the observed-frame $24 \mu\text{m}$ fluxes is shown on the left panel, and the histogram of the observed-frame R -band magnitudes is shown on the right panel. In both panels, the outlined histogram comprises all galaxies in the central XFLS region that are brighter than 0.9 mJy at $24 \mu\text{m}$. The filled histogram corresponds to the sources that were targeted by this program.

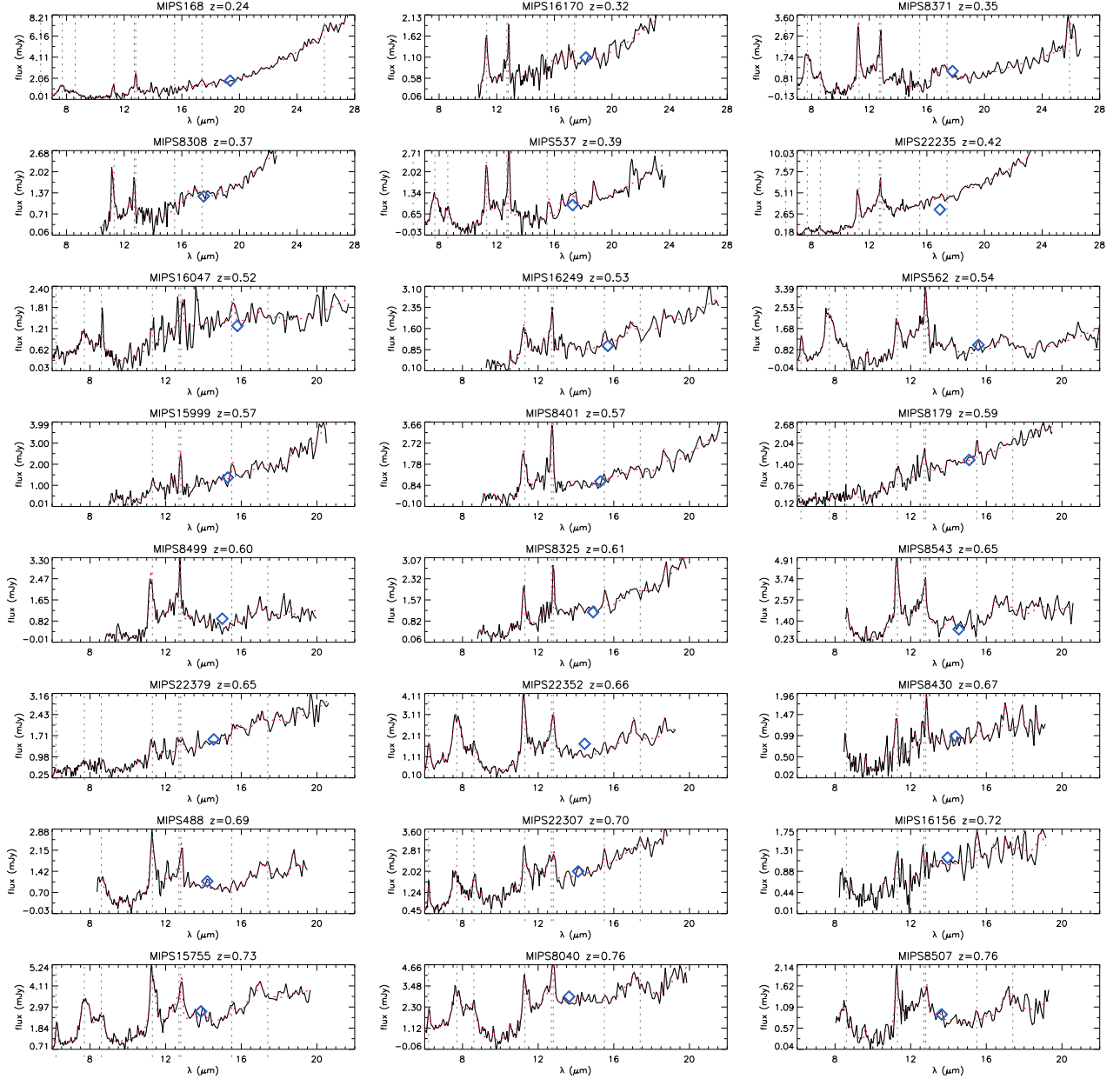


Fig. 3.— Rest-frame IRS spectra of 24- μm selected, IR-luminous galaxies with reliable redshift measurements. These are the sources with confidence classification *a*, *b*, or *c* in Table 2. Each fully reduced spectrum is plotted using a solid line and its best-fit model, computed with PAHFIT, is overplotted using a dashed line. The MIPS 24 μm flux of each source, taken from the Fadda et al. (2006) catalog, is overplotted as a diamond. The dashed vertical lines correspond to the wavelengths where bright features or lines are expected to be, namely, at 6.2, 7.7, 8.6, 11.3, 12.7, 12.8, 15.5, 17.4, and 25.9 μm .

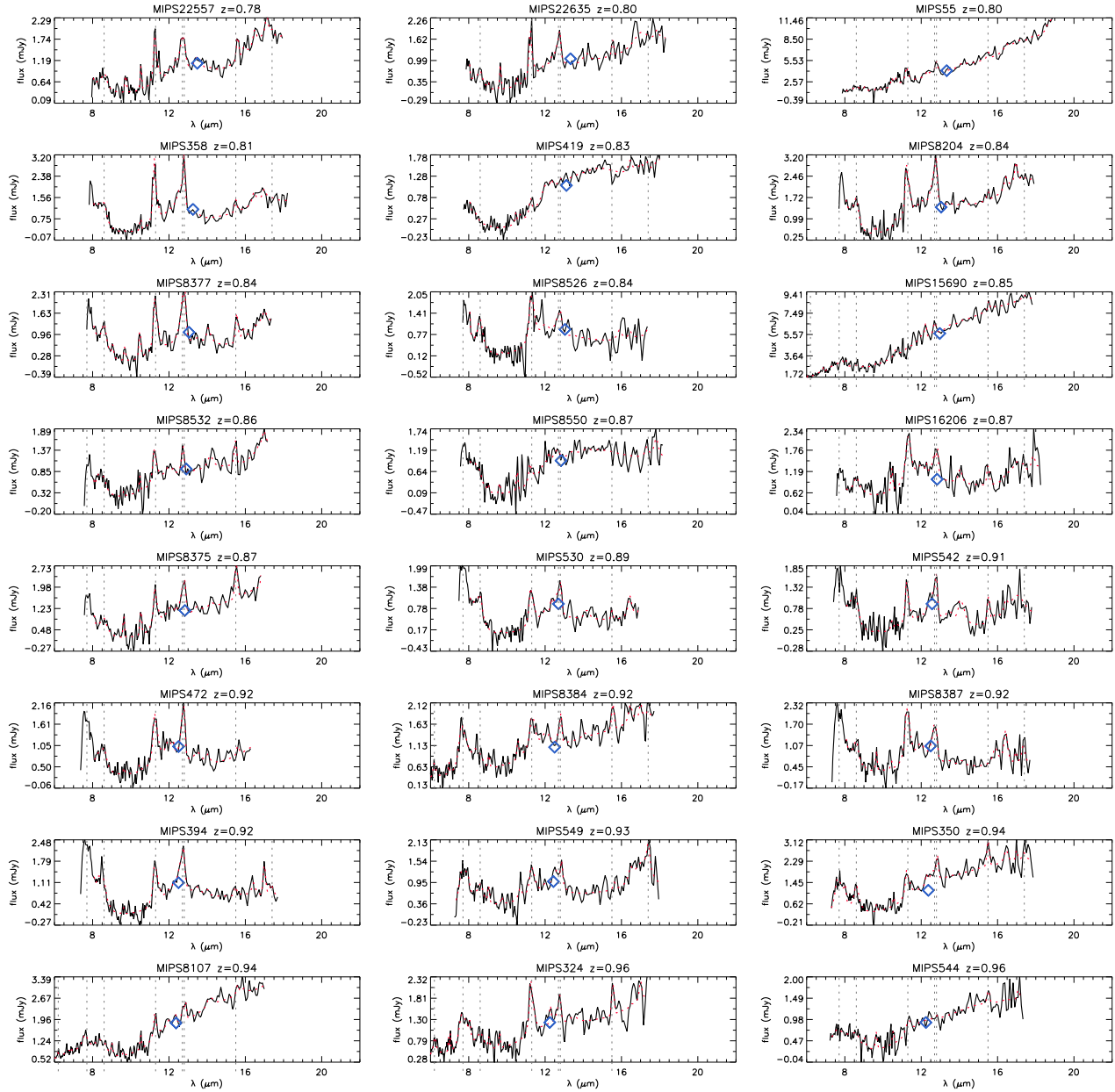


Figure 3— continued.

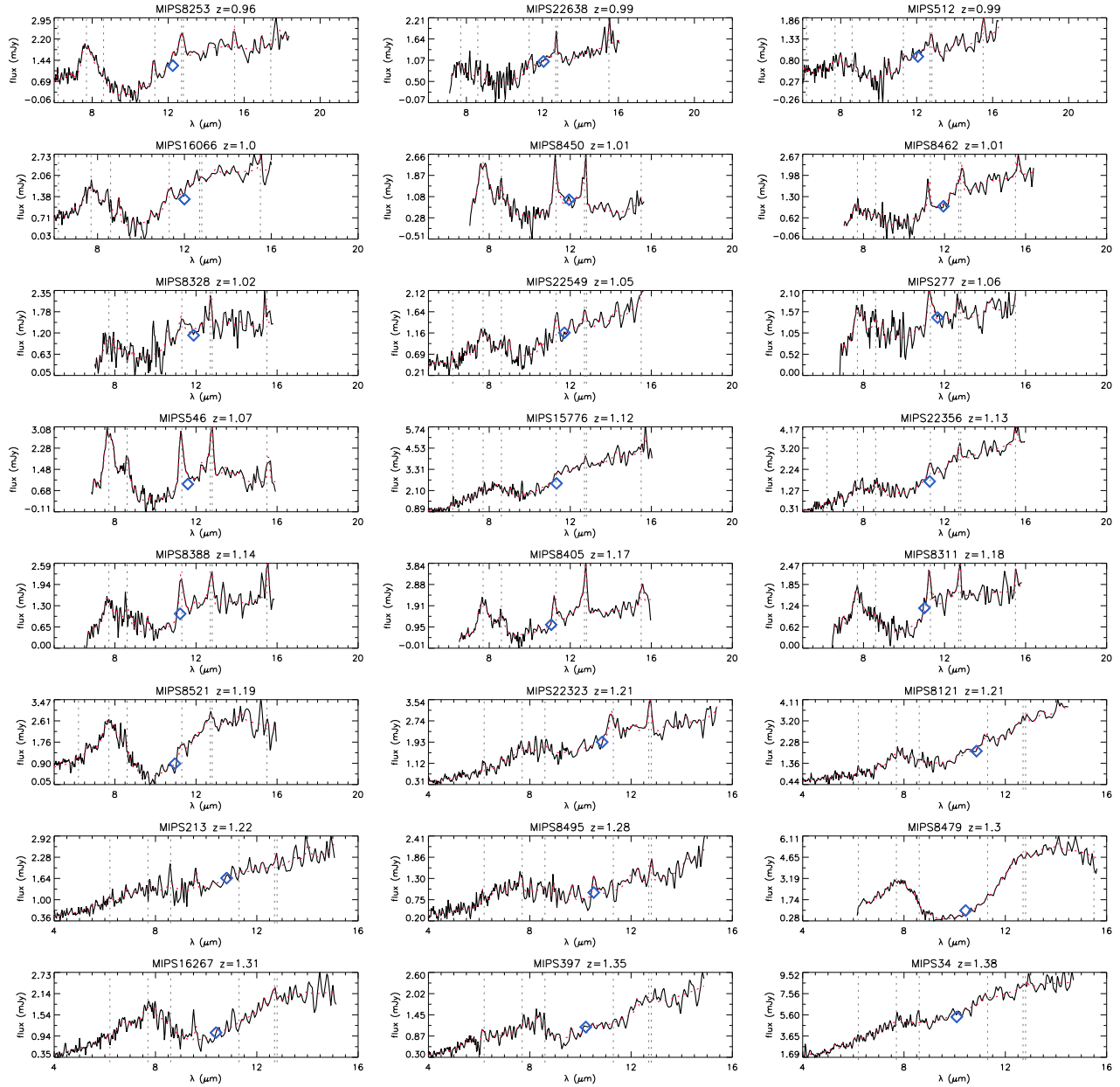


Figure 3— continued.

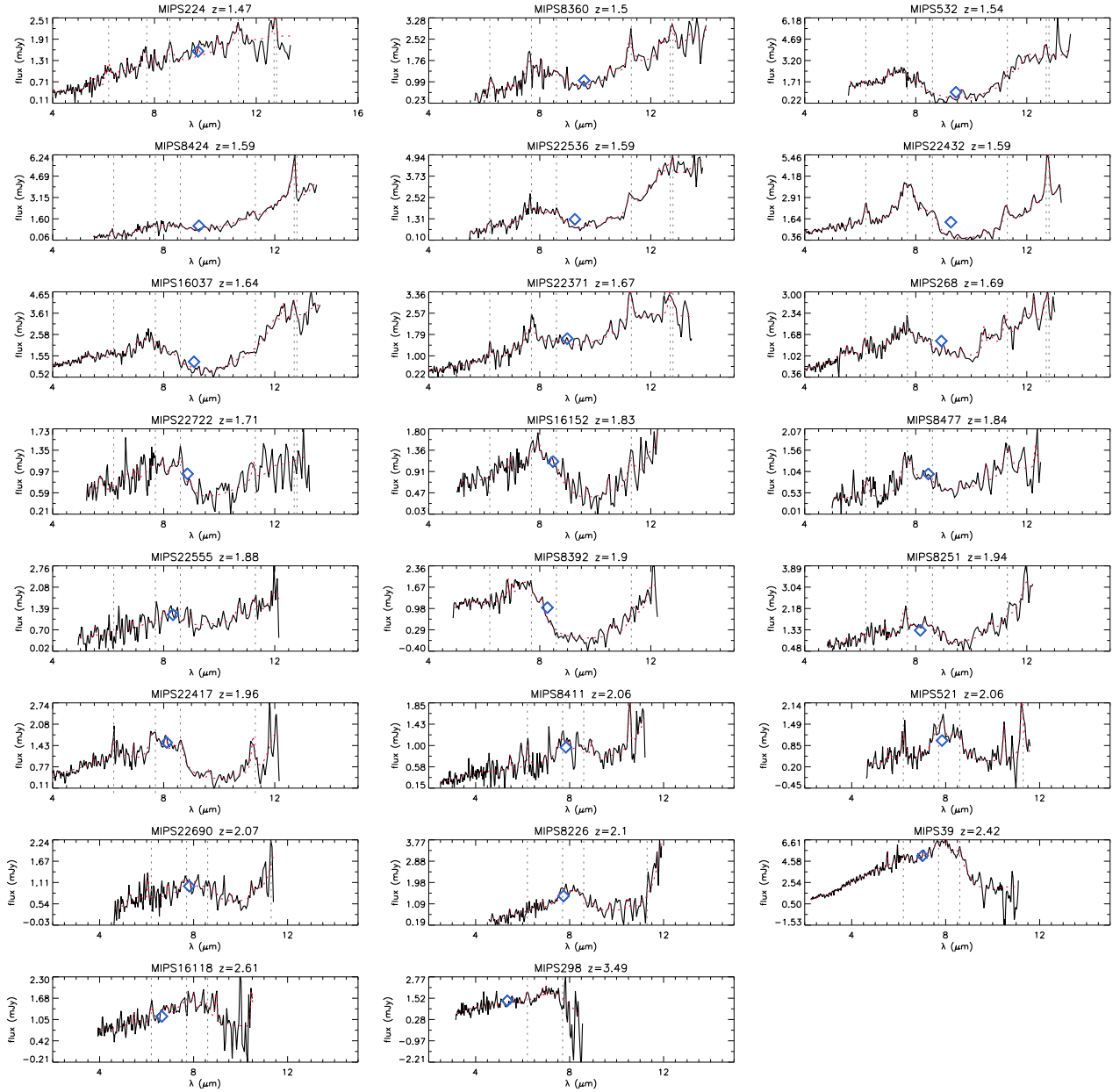


Figure 3— continued.

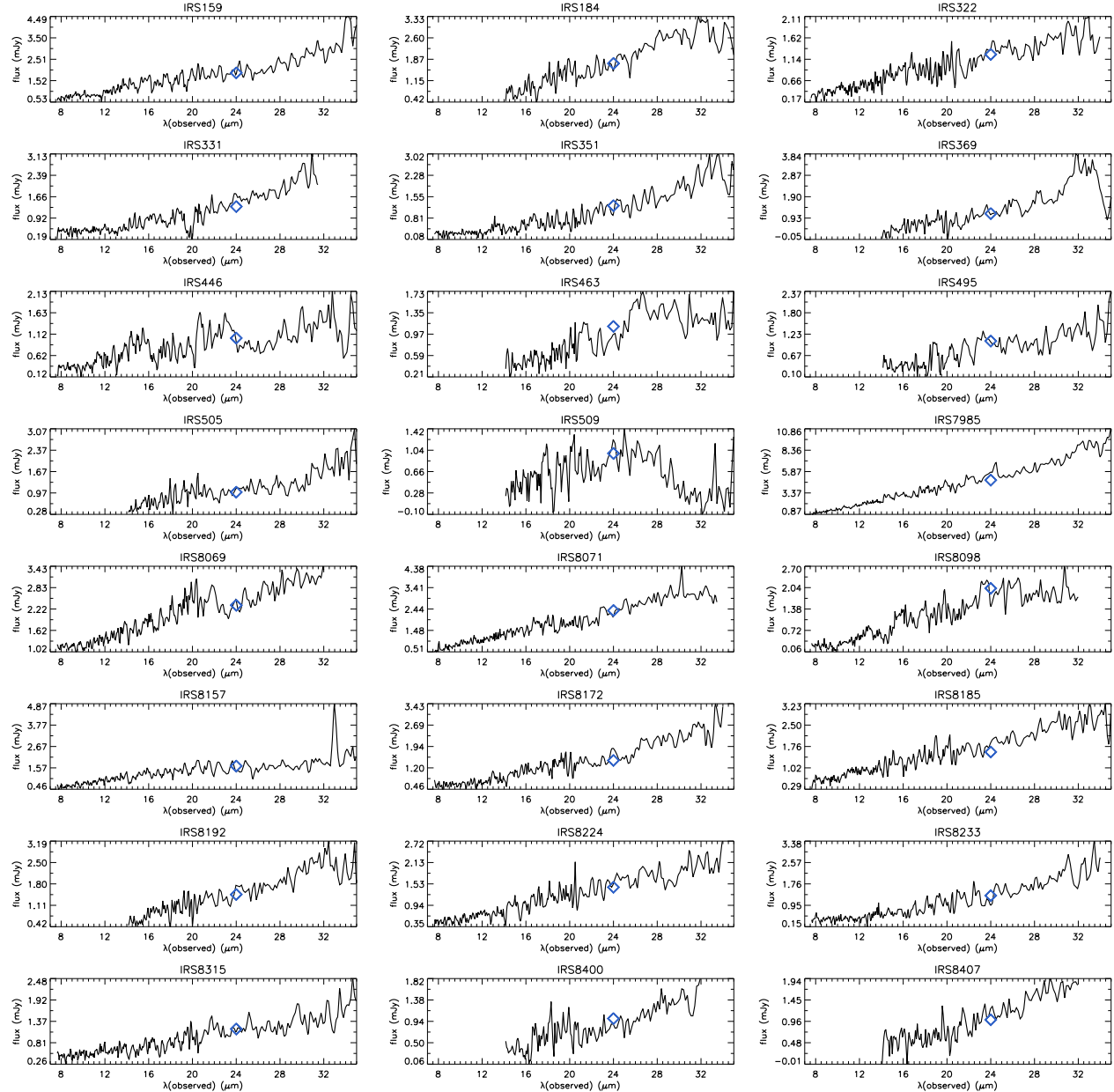


Fig. 4.— Observed-frame IRS spectra of 24- μm selected, IR-luminous galaxies of unknown or uncertain redshift (including sources with confidence classification d , e , or f in Table 2). Each fully reduced spectrum is plotted using a solid line, and its corresponding MIPS 24 μm flux (Fadda et al. 2006) is overplotted as a diamond.

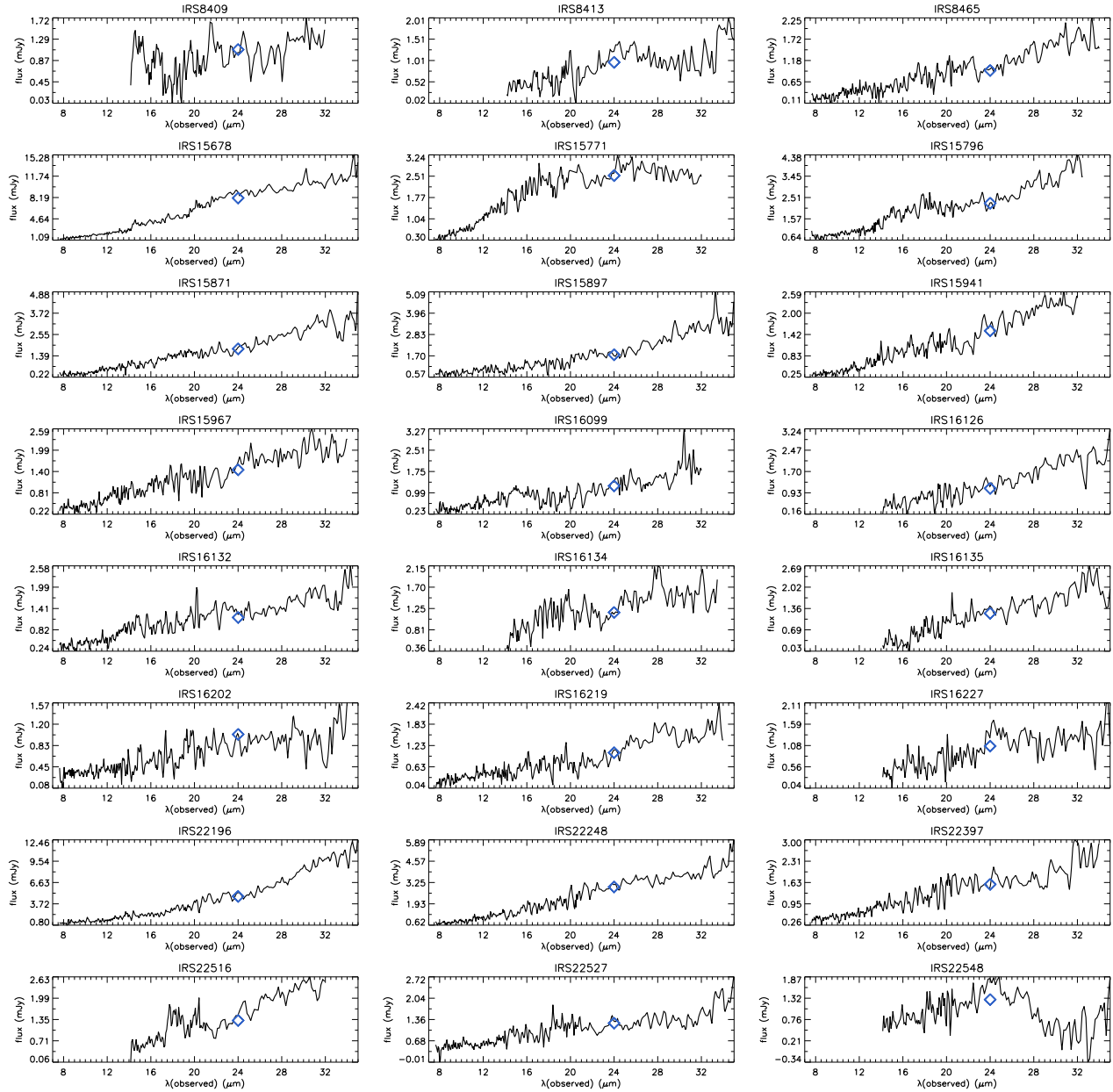


Figure 4— continued.

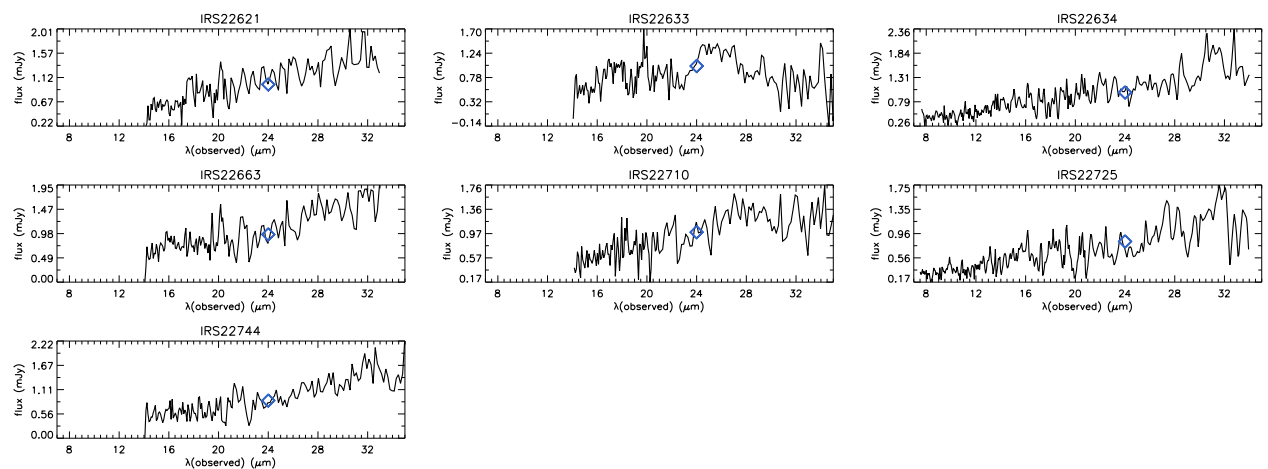


Figure 4— continued.

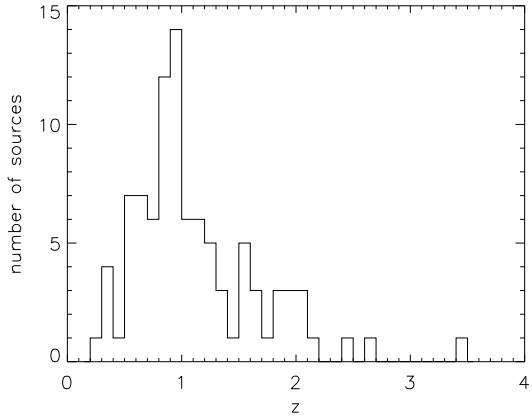


Fig. 5.— Redshift distribution of the 95 sources with reliable z measurements.

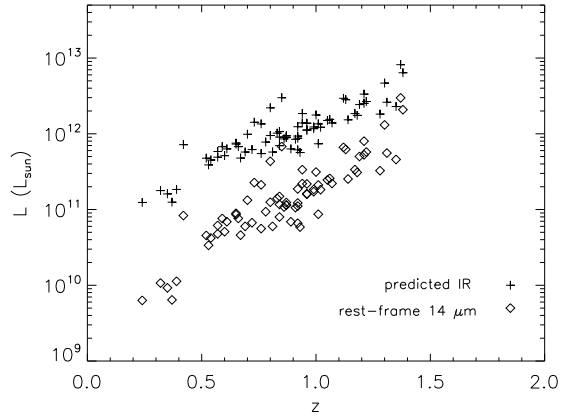


Fig. 6.— Infrared luminosities of the sources with reliable z measurements. The monochromatic, rest-frame $14 \mu\text{m}$ luminosities of these sources are computed from the IRS spectra and are plotted as diamonds. The predicted bolometric IR luminosities (crosses) are estimated based on the relation between L_{14} and L_{IR} presented in Sajina et al. (2008). Most sources are LIRGs at $z < 1$ and ULIRGs at $z \gtrsim 1$.

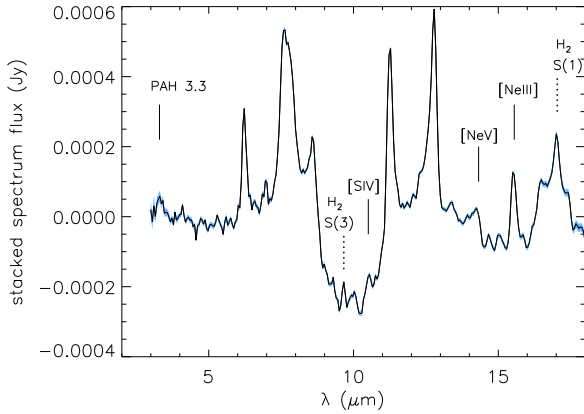


Fig. 7.— Stacked spectrum of sources with [Ne II] detections. Spectral stacking enables the significant detection of the PAH feature at $3.3 \mu\text{m}$, of H₂ lines, and of a line at $14.3 \mu\text{m}$ which is likely to be [Ne V]. The $1-\sigma$ uncertainty around the spectrum is indicated with a filled area.

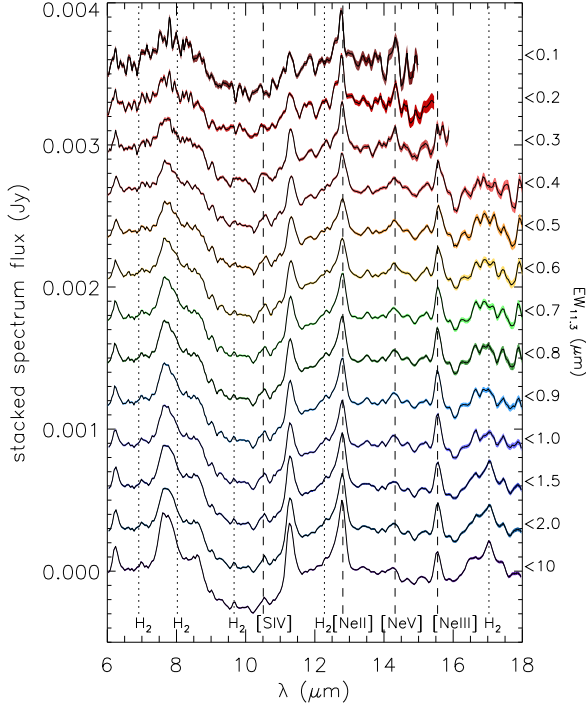


Fig. 8.— Stacked spectra of sources with $11.3\text{ }\mu\text{m}$ PAH detections. Each stacked spectrum was created using sources that have $\text{EW}_{11.3}$ below a certain threshold. We used an $\text{EW}_{11.3}$ threshold that increased from 0.1 to $10\text{ }\mu\text{m}$, leading to spectra that are shown in this figure from top to bottom, respectively. By construction, each stacked spectrum contains all individual galaxy spectra that were included in the computation of the stacked spectra displayed above it. For viewing clarity, an arbitrary constant was set as the continuum of each spectrum. The 1σ uncertainty around each spectrum is indicated with a filled area. The strength of the line at $14.3\text{ }\mu\text{m}$ increases with decreasing $\text{EW}_{11.3}$ and it is highest for AGN-dominated sources, indicating that the emission is mostly originating from the high-ionization [Ne V] line instead of its neighboring [Cl II] line. The H_2 emission is primarily detected in spectra that comprise sources with strong PAH emission.

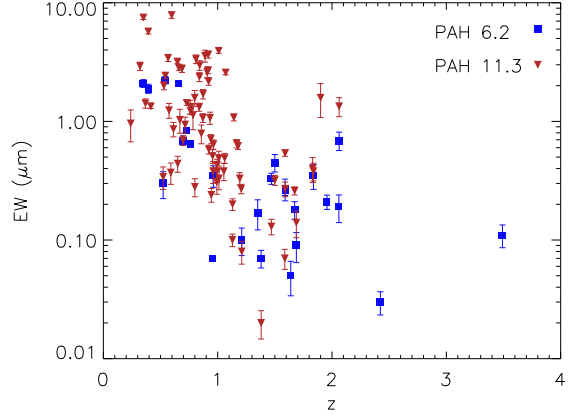


Fig. 9.— Equivalent width of PAH features vs z . The EW decreases with increasing z , indicating a brighter continuum underlying the features.

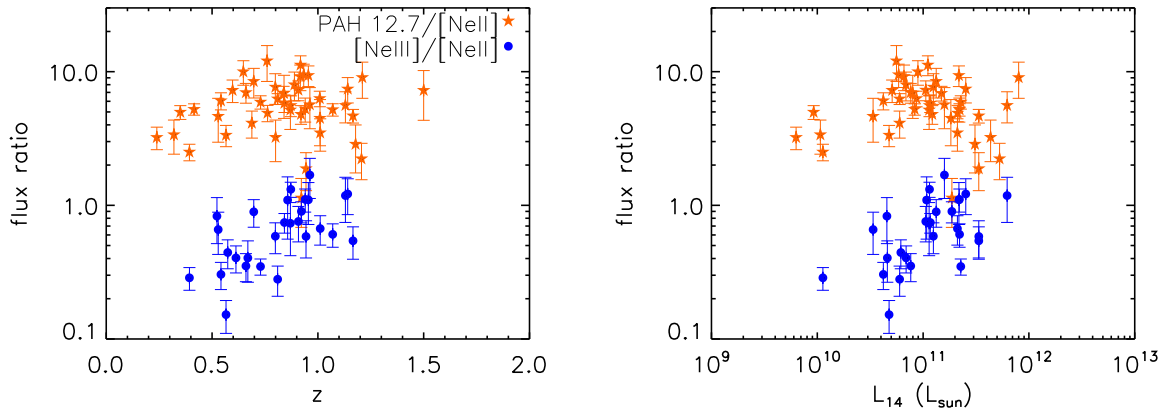


Fig. 10.— Line and feature flux ratios as a function of redshift and 14 μm continuum luminosity. The ratio of the 12.7 μm PAH flux to the [Ne II] flux is independent of redshift or luminosity. However, the [Ne III]/[Ne II] flux ratio increases, implying that the radiation field becomes harder with increasing z and L_{14} .

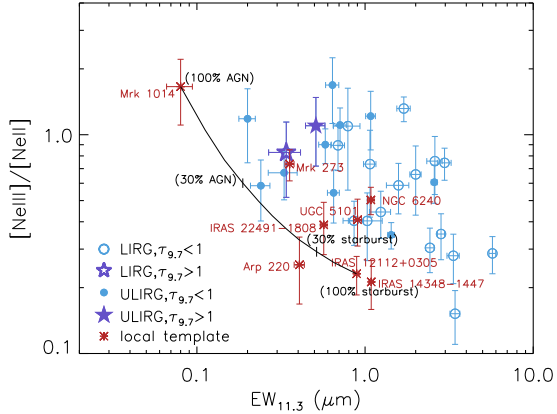


Fig. 11.— Diagnostic diagram for IR-luminous galaxy samples of wide z range. LIRGs are plotted with open symbols and ULIRGs are plotted with filled symbols. Circles are used for sources with $\tau_{9.7} < 1$, while five-pointed stars are used for sources with $\tau_{9.7} \geq 1$. Local galaxy templates are plotted as plain stars. The solid line indicates how the position of a source changes when the fraction of AGN or starburst contribution to L_{14} increases from 0% to 100%. For this reason, we used Mrk 1014 as an AGN template and IRAS 12112+0305 as a starburst template. The radiation field in many distant star-forming sources is harder than that in their local analogues. Moreover, their $EW_{11.3}$ values are often higher than those of local ULIRGs.

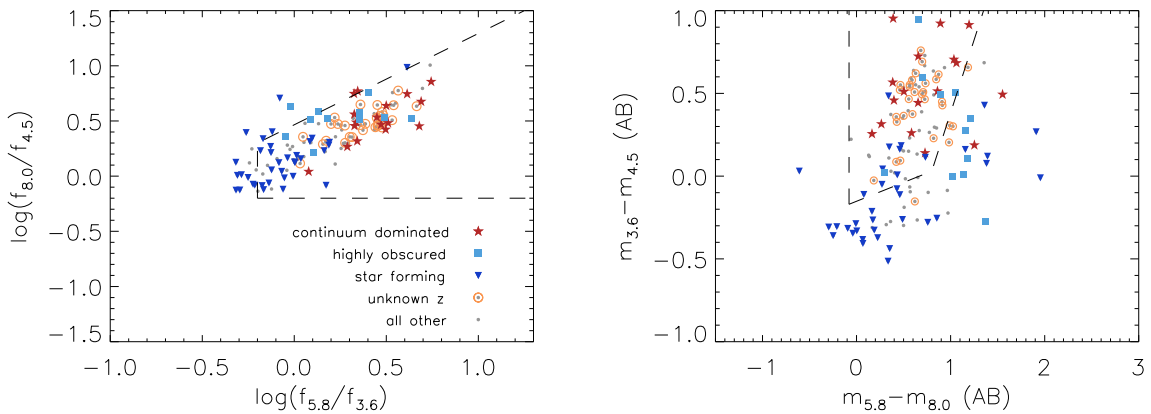


Fig. 12.— Comparison between the IRS spectral classification and the position of sources on (observed-frame) color-color diagrams that are used for the selection of AGN based on broad-band IR data (Lacy et al. 2004, left panel; Stern et al. 2005, right panel). In both panels, the dashed line sets the limits of the AGN wedge. The criterion used for the classification of continuum-dominated sources (stars) and star-forming sources (triangles) was that the $EW_{11.3}$ is ≤ 0.1 and $> 0.8 \mu m$, respectively. Obscured systems with $\tau_{9.7} \geq 1$ (and $EW < 0.8 \mu m$) are plotted as squares. While most sources with a continuum-dominated IRS spectrum lie inside the AGN wedge, so does a large fraction of star-forming and highly-obscured systems.

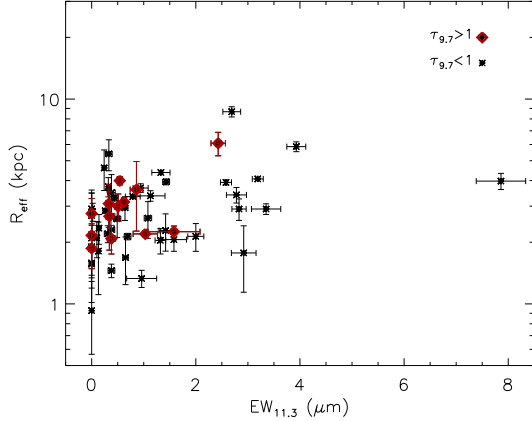


Fig. 13.— Effective radii of IR-luminous galaxies in the rest-frame optical or NIR wavelengths vs EW of their $11.3\text{ }\mu\text{m}$ PAH emission. The strongest starbursts, i.e., the sources with $\text{EW}_{11.3}>2\text{ }\mu\text{m}$, are typically more extended than ~ 3 kpc. The radial extent of the sources that are heavily obscured in the MIR can also be large.

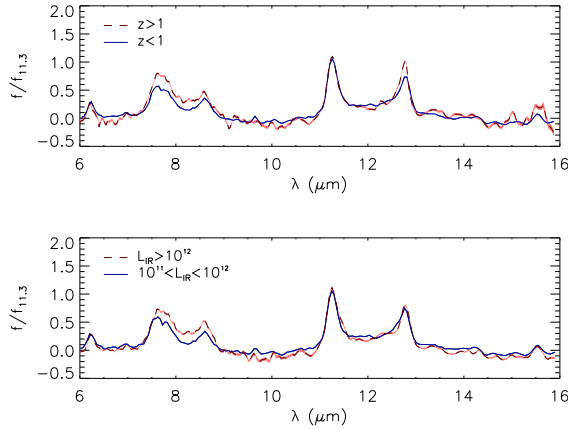


Fig. 14.— Stacked spectra of sources in different redshift and luminosity bins are shown in the top and bottom panels, respectively. The stacked spectrum of sources at $z<1$ or $L_{\text{IR}}<10^{12} L_{\odot}$ is plotted with a solid line and that of sources at $z\geq 1$ or $L_{\text{IR}}\geq 10^{12} L_{\odot}$ is plotted with a dashed line. The filled area around each spectrum corresponds to its 1σ uncertainty. All individual spectra were extinction corrected, continuum subtracted, and normalized at the peak of the $11.3\text{ }\mu\text{m}$ feature so that changes in the relative shape of features can be investigated. For this reason, the stacked spectra were created using all sources with rest-frame $11.3\text{ }\mu\text{m}$ data. We observe significant but small differences in the PAH flux ratios with z or L .

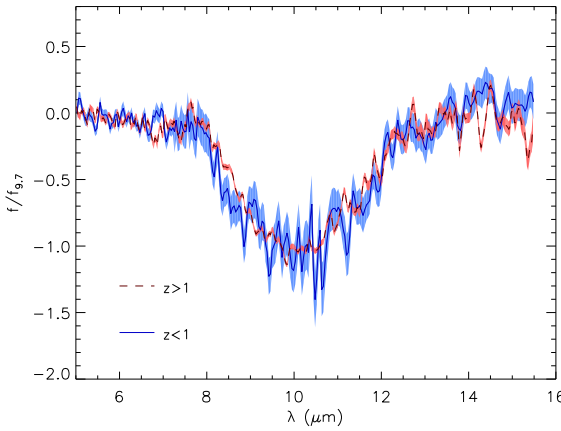


Fig. 15.— Stacked extinction curve spectra. The spectra for $z < 1$ and $z \geq 1$ are plotted with a solid line and a dashed line, respectively. The filled area around each spectrum corresponds to its 1σ uncertainty. We removed the continuum and emission features of each spectrum and divided it by its $9.7 \mu\text{m}$ flux prior to computing the stacked spectrum in order to investigate for differences in the extinction properties with z . We used sources with rest-frame $9.7 \mu\text{m}$ data that have moderate or high obscuration, i.e., $\tau_{9.7} \geq 0.5$, and $\text{EW}_{11.3} < 0.8 \mu\text{m}$ to avoid starbursts that could have emission-line residuals affecting the shape of the silicate absorption. We find no significant ($>3\sigma$) change in the extinction curve properties with z .

TABLE 1

COORDINATES, INTEGRATION TIMES, AND PHOTOMETRIC PROPERTIES OF THE SOURCES.

Galaxy (1)	coordinates (J2000) (2)	tint(SL1, LL2, LL1) (s) (3)	m _R (Vega) (4)	f _{3.6} (μJy) (5)	f _{4.5} (μJy) (6)	f _{5.8} (μJy) (7)	f _{8.0} (μJy) (8)	f ₂₄ (mJy) (9)	R _{eff} (kpc) (10)
MIPS34	17:17:08.7+59:13:41.1	483, 487, 487	21.05	445.8 ± 45.1	680.1 ± 68.5	980.4 ± 100.6	1413.9 ± 142.9	5.42 ± 0.06	2.82 ± 0.28
MIPS39	17:17:50.7+58:47:45.3	483, 487, 731	23.27	58.3 ± 6.7	135.2 ± 15.0	322.9 ± 36.6	971.9 ± 100.7	5.10 ± 0.07	...
MIPS55	17:15:06.6+58:39:39.7	..., 487, 487	20.75	189.8 ± 19.4	144.3 ± 15.3	174.1 ± 20.6	275.8 ± 30.6	4.13 ± 0.06	...
MIPS159	17:13:33.4+59:27:47.2	483, 1462, 1706	22.08	168.7 ± 17.5	277.6 ± 28.7	499.8 ± 53.6	841.1 ± 87.4	1.88 ± 0.06	...
MIPS168	17:17:55.1+59:28:45.3	483, 975, 1218	20.18	96.4 ± 10.8	95.5 ± 11.2	80.4 ± 16.1	486.2 ± 52.0	1.82 ± 0.06	1.33 ± 0.13
MIPS184	17:14:04.5+59:03:03.7	..., 1462, 1706	21.56	130.6 ± 14.1	113.4 ± 12.9	145.6 ± 22.3	257.7 ± 30.9	1.73 ± 0.06	...
MIPS213	17:13:35.7+59:27:21.8	483, 1462, 1706	23.42	34.3 ± 3.9	65.6 ± 7.4	140.7 ± 16.9	365.0 ± 38.8	1.65 ± 0.06	1.90 ± 0.52
MIPS224	17:16:55.8+59:25:40.4	483, 1462, 1706	20.54	149.6 ± 16.0	248.7 ± 26.0	276.5 ± 35.1	493.1 ± 52.7	1.57 ± 0.06	1.81 ± 0.70
MIPS268	17:12:08.9+59:30:25.0	483, 1462, 1706	22.93	59.7 ± 7.0	116.9 ± 12.5	187.7 ± 25.2	366.2 ± 39.3	1.48 ± 0.06	2.34 ± 0.39
MIPS277	17:14:20.8+58:55:02.5	..., 1462, 1706	21.31	134.4 ± 14.2	105.3 ± 11.1	76.7 ± 14.7	139.0 ± 16.3	1.43 ± 0.06	...
MIPS298	17:14:48.9+59:28:47.4	..., 1462, 1706	23.95	<6.5 g	<10.5 g	41.2 ± 12.8	163.5 ± 21.6	1.37 ± 0.06	...
MIPS322	17:14:24.9+59:29:48.0	483, 1462, 1706	23.40	81.6 ± 9.2	131.8 ± 14.7	277.6 ± 34.8	424.2 ± 46.1	1.25 ± 0.06	...
MIPS324	17:17:15.7+59:06:03.3	483, 1462, 1706	20.79	171.9 ± 18.2	211.1 ± 22.4	286.9 ± 35.6	271.8 ± 32.0	1.23 ± 0.06	2.94 ± 0.39
MIPS331	17:15:05.7+59:18:20.3	483, 1462, 1706	22.04	161.8 ± 17.2	200.1 ± 21.3	270.8 ± 32.9	455.4 ± 49.0	1.32 ± 0.07	...
MIPS350	17:15:10.7+59:23:15.9	..., 1462, 1706	22.85	102.5 ± 10.8	86.2 ± 10.0	100.3 ± 14.5	159.8 ± 21.9	1.15 ± 0.06 d	...
MIPS351	17:16:59.2+59:08:11.7	483, 1462, 1706	22.04	104.5 ± 11.6	146.2 ± 15.8	209.2 ± 27.8	331.9 ± 36.8	1.24 ± 0.06	...
MIPS358	17:18:07.1+59:29:37.4	..., 1462, 1706	22.24	108.5 ± 11.5	76.3 ± 8.3	81.7 ± 13.8	86.8 ± 11.7	1.11 ± 0.05	2.91 ± 0.17
MIPS369	17:14:50.9+59:26:33.3	..., 1462, 1706	22.32	94.5 ± 10.2	93.8 ± 10.7	58.7 ± 11.8	106.9 ± 17.3	1.13 ± 0.06	...
MIPS394	17:13:15.7+59:12:08.5	..., 1462, 1706	22.08	134.0 ± 14.0	105.3 ± 12.1	69.2 ± 12.6	108.5 ± 17.4	1.10 ± 0.06	...
MIPS397	17:15:05.9+59:09:16.9	966, 2924, 3412	23.80	65.2 ± 7.7	74.2 ± 8.6	138.1 ± 20.9	270.0 ± 30.1	1.12 ± 0.06	2.79 ± 0.69
MIPS419	17:15:45.2+59:05:38.7	..., 2924, 3412	22.85	33.1 ± 4.6	42.6 ± 6.0	83.8 ± 16.6	243.7 ± 29.6	1.06 ± 0.06	1.87 ± 0.38
MIPS446	17:14:09.0+59:17:48.4	483, 1462, 1706	21.82	142.7 ± 14.8	140.7 ± 14.7	175.6 ± 21.2	283.3 ± 30.8	1.03 ± 0.06	...
MIPS463	17:14:45.2+58:54:55.1	..., 2924, 3412	...	44.3 ± 6.0 h	58.2 ± 7.4 h	78.9 ± 16.1	169.1 ± 21.4 h	1.11 ± 0.06	...
MIPS472	17:18:16.7+59:19:36.1	..., 1462, 1706	22.21	70.7 ± 16.0 d, i	41.7 ± 13.1 d, i	<32.9 g	62.0 ± 12.6	1.03 ± 0.06	...
MIPS488	17:15:11.9+58:49:35.0	..., 2924, 3412	21.16	119.2 ± 12.7	88.3 ± 10.1	98.4 ± 16.4	116.9 ± 16.4	1.08 ± 0.06	3.40 ± 0.30
MIPS495	17:14:33.0+58:58:19.8	..., 1462, 1706	21.84 b	159.3 ± 16.9	155.6 ± 16.9	171.4 ± 23.9	202.8 ± 25.1	1.05 ± 0.06	...
MIPS505	17:15:59.4+59:27:33.4	..., 1462, 1706	24.91	17.2 ± 2.8	31.5 ± 5.4	63.1 ± 11.5	187.8 ± 23.8	1.00 ± 0.06	...
MIPS509	17:14:22.1+59:28:14.3	..., 1462, 1706	...	<6.9 g	17.3 ± 3.9	<36.3 g	136.4 ± 20.0	0.98 ± 0.06	...
MIPS512	17:16:55.7+59:10:46.1	483, 1462, 1706	23.21	117.7 ± 12.7	162.7 ± 17.4	173.4 ± 24.0	272.0 ± 31.1	0.89 ± 0.06	2.19 ± 0.21
MIPS521	17:13:41.4+58:57:03.7	..., 1462, 1706	...	64.5 ± 7.4 d, i	75.8 ± 8.4 d, i	93.7 ± 19.6 d, i	129.1 ± 18.7 d, i	1.00 ± 0.06	...
MIPS530	17:13:37.1+58:46:37.5	..., 2924, 3412	22.18	120.4 ± 12.7	123.8 ± 8.6 g	179.2 ± 21.2 g	102.291 ± 16.1 g	0.91 ± 0.06	...
MIPS532	17:15:26.1+58:56:32.4	..., 2924, 3412	22.70	51.5 ± 6.7	56.9 ± 7.5	62.9 ± 15.1	185.8 ± 23.1	0.98 ± 0.06	...
MIPS537	17:17:59.3+59:21:56.3	483, 1462, 1706	19.90 a, b	88.7 ± 10.1	113.6 ± 12.6	48.6 ± 14.1	282.2 ± 32.5	0.94 ± 0.06	...
MIPS542	17:12:45.7+59:32:14.4	..., 1462, 1706	22.06	119.7 ± 13.0	108.1 ± 12.1	87.2 ± 16.8	93.6 ± 15.4	0.90 ± 0.05	...
MIPS544	17:13:07.7+58:44:13.3	..., 1706, 1950	23.03	49.0 ± 5.8	67.7 ± 8.2	74.2 ± 13.4	227.2 ± 28.2	0.91 ± 0.06	2.08 ± 0.33
MIPS546	17:12:16.1+59:11:22.0	..., 1462, 1706	22.08	172.5 ± 18.1	141.8 ± 15.0	103.0 ± 17.7	119.7 ± 15.9	0.93 ± 0.06	3.92 ± 0.11
MIPS549	17:16:28.9+59:29:21.0	..., 1462, 1706	21.54	80.2 ± 9.1	62.8 ± 7.8	82.6 ± 15.3	96.8 ± 16.5	0.98 ± 0.05	...
MIPS562	17:12:39.6+58:59:55.1	483, 1462, 1706	20.90	214.0 ± 43.8 d, i	165.5 ± 24.8 d, i	140.2 ± 21.8	281.6 ± 31.2	1.01 ± 0.06	6.08 ± 0.80
MIPS7985	17:13:25.5+60:07:20.2	483, 487, 487	22.57	168.6 ± 17.5	269.1 ± 28.1	493.1 ± 53.0	947.0 ± 98.5	4.87 ± 0.06	...
MIPS8040	17:13:12.0+60:08:40.2	483, 731, 975	...	j	... j	352.1 ± 41.7	529.6 ± 54.9	2.88 ± 0.07	...
MIPS8069	17:15:00:45+59:11:17	483, 975, 975	19.12 c	386.9 ± 39.2	545.3 ± 54.8 e	695.0 ± 72.6	972.0 ± 97.8 e	2.33 ± 0.03	...
MIPS8071	17:12:43.5+60:06:50.0	483, 1462, 1706	22.10	120.8 ± 13.0	216.9 ± 22.9	368.8 ± 41.9	782.4 ± 82.3	2.38 ± 0.06	...
MIPS8098	17:16:08.0+60:06:38.8	483, 1462, 1706	21.83	167.8 ± 17.8	194.5 ± 20.2	189.1 ± 25.3	292.6 ± 31.9	2.02 ± 0.06	...
MIPS8107	17:16:38.7+59:49:44.5	483, 1462, 1706	22.17	104.1 ± 10.6 e	132.8 ± 13.5 e	217.8 ± 23.1 e	449.2 ± 45.0 e	1.84 ± 0.03	4.61 ± 1.03
MIPS8121	17:13:22.8+60:10:44.6	483, 1462, 1706	23.43	153.4 ± 31.5 d, i	258.7 ± 41.2 d, i	481.4 ± 53.8	685.9 ± 73.1	1.89 ± 0.06	...
MIPS8157	17:18:40.6+60:09:35.3	483, 1462, 1706	23.31	123.5 ± 12.7	189.6 ± 19.9	226.4 ± 30.1	563.4 ± 58.5	1.66 ± 0.06	...
MIPS8172	17:16:49.1+59:49:18.6	483, 1462, 1706	23.06	142.9 ± 15.3	138.6 ± 14.9	473.1 ± 53.2	798.7 ± 83.0 f	1.46 ± 0.03	...
MIPS8177	17:16:10.5+60:13:32.4	483, 1462, 1706	20.87	123.5 ± 13.4	123.8 ± 14.9	243.6 ± 31.5	274.2 ± 30.8	1.53 ± 0.06	2.68 ± 0.52
MIPS8185	17:14:22.8+60:28:34.6	483, 1218, 1462	23.80	87.5 ± 9.7	149.9 ± 15.8	262.4 ± 33.5	572.0 ± 59.1	1.57 ± 0.06 d	...
MIPS8192	17:12:53.9+60:05:00:8	..., 1462, 1706	23.09	52.3 ± 5.9	63.1 ± 7.2	86.6 ± 13.7	214.2 ± 24.9	1.46 ± 0.06	...
MIPS8204	17:14:40.9+59:58:19.2	..., 1462, 1706	22.83	163.1 ± 16.8	152.0 ± 15.8	149.9 ± 19.5	222.6 ± 24.8	1.39 ± 0.03	2.04 ± 0.29
MIPS8224	17:16:49.0+59:53:35.5	483, 1462, 1706	23.53	94.5 ± 9.6 e	167.6 ± 17.1 e	206.9 ± 27.4 e	465.5 ± 47.1 e	1.44 ± 0.03	...
MIPS8226	17:12:04.7+60:16:32.0	..., 1462, 1706	20.95	30.3 ± 4.3	72.8 ± 8.3	144.6 ± 22.2	206.9 ± 23.9	1.42 ± 0.06	0.93±0.36
MIPS8233	17:17:31.5+59:40:33.8	483, 1462, 1706	21.92	143.0 ± 14.4 e	198.8 ± 20.2 e	270.0 ± 28.2 e	398.8 ± 40.5 e	1.32 ± 0.03	...
MIPS8251	17:12:17.2+7:60:03:33:6	..., 1462, 1706	23.22	28.2 ± 4.2	44.5 ± 5.8	59.6 ± 14.8	249.0 ± 28.8	1.31 ± 0.06	2.10 ± 0.76
MIPS8253	17:15:07.8+60:13:52.9	483, 1462, 1706	21.78	113.4 ± 12.4	114.4 ± 12.7	154.1 ± 22.3	440.4 ± 47.0	1.25 ± 0.06	2.99 ± 0.45
MIPS8308	17:16:34.4+60:15:44.0	..., 1462, 1706	20.29	89.4 ± 10.1	96.0 ± 10.8	67.8 ± 15.5	242.2 ± 28.0	1.26 ± 0.06	2.28 ± 0.47
MIPS8311	17:15:27.7+60:07:26.3	..., 1462, 1706	22.08	100.4 ± 11.2	100.2 ± 11.3	89.6 ± 17.7	229.1 ± 28.5	1.17 ± 0.06	3.15 ± 0.15
MIPS8315	17:13:57.0+59:44:37.6	483, 1462, 1706	23.88	80.6 ± 9.3	135.2 ± 15.0	245.7 ± 29.7	482.7 ± 51.8	1.17 ± 0.04	...
MIPS8325	17:16:43.7+60:20:13.6	..., 1462, 1706	21.05	69.8 ± 8.0	62.9 ± 7.6	84.9 ± 16.8	129.6 ± 18.1	1.13 ± 0.06	3.61 ± 1.34
MIPS8328	17:16:06:7+59:44:54.6	..., 1462, 1706	22.33	95.5 ± 9.7 e	89.9 ± 9.4 e	76.9 ± 9.3 e	129.5 ± 14.1 e	1.14 ± 0.03	2.60 ± 0.49
MIPS8360	17:16:52.5+59:35:31.9	..., 1462, 1706	22.07	96.7 ± 9.8 e	107.0 ± 11.2 e	88.1 ± 10.5 e	120.9 ± 13.1 e	1.04 ± 0.03	3.73 ± 0.40
MIPS8371	17:13:25.0+59:45:57.8	483, 1462, 1706	20.03 b, c	176.8 ± 39.2 d, i	205.2 ± 19.6 d, i	131.5 ± 18.4	381.6 ± 24.5 d, i	1.12 ± 0.06	...
MIPS8375	17:14:33.8+59:52:21.8	..., 1462, 1706	21.06 b, c	143.5 ± 4.7 h, g	144.5 ± 5.9 h, g, e	72.6 ± 16.0 d	108.2 ± 12.2 e, d	1.16 ± 0.03 d	...
MIPS8377	17:17:33.5+59:46:40.7	..., 1462, 1706	22.17 b	101.7 ± 33.1 d, i, e	76.8 ± 22.4 d, i, e	89.9 ± 9.8 e	74.1 ± 8.4 e, d	1.03 ± 0.03	...
MIPS8384	17:16:47.5+60:17:57.2	483, 1462, 1706	22.39	232.3 ± 23.7	238.8 ± 24.6	242.8 ± 27.7	340.1 ± 36.4	1.09 ± 0.06	...
MIPS8387	17:18:02.8+60:15:22.0	..., 1462, 1706	21.33 a, c	280.1 ± 28.8	201.1 ± 21.2	190.8 ± 26.2	151.7 ± 20.5	1.06 ± 0.06	8.67 ± 0.50
MIPS8388	17:14:00.4+60:14:09.5	..., 1462, 1706	21.42	112.4 ± 12.3	130.6 ± 14.2	113.4 ± 18.9	173.1 ± 21.6	1.05 ± 0.06	2.62 ± 0.53
MIPS8392	17:13:43.9+59:57:14.5	..., 2924, 3412	...	15.5 ± 2.7	23.1 ± 4.3	63.7 ± 12.6	223.0		

TABLE 1—Continued

Galaxy (1)	coordinates (J2000) (2)	t_{int} (SL1, LL2, LL1) (s) (3)	m_R (Vega) (4)	$f_{3.6}$ (μJy) (5)	$f_{4.5}$ (μJy) (6)	$f_{5.8}$ (μJy) (7)	$f_{8.0}$ (μJy) (8)	f_{24} (mJy) (9)	R_{eff} (kpc) (10)
MIPS8499	17:12:16.5+59:57:10.9	..., 1462, 1706	20.51	261.2 \pm 26.9	192.6 \pm 19.8	159.3 \pm 20.8	159.7 \pm 18.7	0.91 \pm 0.06	3.98 \pm 0.36
MIPS8507	17:13:29.9+59:44:34.2	..., 1706, 1950	20.89	150.5 \pm 15.8	113.4 \pm 12.8	148.3 \pm 20.8	112.9 \pm 17.7	0.91 \pm 0.06	4.38 \pm 0.02
MIPS8521	17:12:18.9+60:10:03.8	483, 1462, 1706	...	107.6 \pm 11.7	169.3 \pm 18.0	243.4 \pm 29.6	555.4 \pm 58.2	0.89 \pm 0.06	3.09 \pm 0.73
MIPS8526	17:16:28.4+59:44:22.9	..., 1462, 1706	22.44	131.5 \pm 13.3 ^e	98.4 \pm 10.4 ^e	88.0 \pm 10.4 ^e	80.7 \pm 9.5 ^e	0.92 \pm 0.03	...
MIPS8532	17:16:23.3+59:36:46.9	..., 1462, 1706	21.73	93.1 \pm 9.5 ^e	69.9 \pm 7.3 ^e	62.8 \pm 8.2 ^e	73.2 \pm 8.5 ^e	0.91 \pm 0.03	3.34 \pm 0.04
MIPS8543	17:18:12.7+59:39:22.6	..., 1462, 1706	20.65	96.3 \pm 9.8 ^e	73.9 \pm 7.8 ^e	82.2 \pm 10.0 ^e	81.7 \pm 9.6 ^e	0.94 \pm 0.03	4.07 \pm 0.02
MIPS8550	17:18:14.6+59:56:05.7	..., 1462, 1706	22.66	76.1 \pm 8.9	59.2 \pm 6.4 ^e	72.5 \pm 15.9	255.5 \pm 26.4 ^e	0.92 \pm 0.04	...
MIPS15673	17:23:28.4+59:29:47.3	483, 487, 487	22.15	339.9 \pm 14.1 ^{d,i}	612.2 \pm 62.3	972.4 \pm 102.6	1699.6 \pm 172.6	8.10 \pm 0.07	...
MIPS15690	17:19:22.4+60:14:56.2	483, 487, 487	22.20	125.4 \pm 13.6	149.1 \pm 16.3	277.3 \pm 34.8	879.1 \pm 91.6	5.66 \pm 0.07	2.91 \pm 0.69
MIPS15755	17:18:34.9+59:45:34.1	483, 731, 975	20.72	262.0 \pm 26.3 ^e	272.7 \pm 27.6 ^e	403.9 \pm 41.0 ^e	521.5 \pm 53.0 ^e	2.74 \pm 0.03	3.94 \pm 0.13
MIPS15771	17:20:11.4+59:36:00.9	483, 731, 975	24.00	20.3 \pm 3.2	38.2 \pm 4.8	111.1 \pm 18.0	387.5 \pm 41.3	2.53 \pm 0.03	...
MIPS15776	17:20:50.7+59:32:54.6	483, 1462, 1706	22.19	204.8 \pm 21.5	328.0 \pm 33.8	607.2 \pm 66.0	965.3 \pm 99.8	2.51 \pm 0.06	2.10 \pm 0.42
MIPS15796	17:18:44.9+60:00:26.2	483, 731, 975	24.16	191.3 \pm 19.5	313.1 \pm 32.0	520.4 \pm 54.0	822.9 \pm 84.7	2.26 \pm 0.06	...
MIPS15871	17:19:17.3+59:29:29.3	483, 1462, 1706	23.26	48.7 \pm 6.0	98.0 \pm 11.0	225.0 \pm 30.3	422.1 \pm 45.7	1.77 \pm 0.05	...
MIPS15897	17:20:17.0+59:27:33.1	483, 1462, 1706	22.20	129.8 \pm 13.6	223.9 \pm 23.6	380.5 \pm 42.6	647.7 \pm 67.6	1.76 \pm 0.05	...
MIPS15941	17:22:47.8+60:09:46.7	483, 1462, 1706	23.44	52.9 \pm 6.8 ^{d,i}	97.9 \pm 14.9 ^{d,i}	162.6 \pm 20.8	316.7 \pm 30.3 ^{f,i}	1.52 \pm 0.06	...
MIPS15967	17:19:24.7+59:28:58.7	483, 1462, 1706	20.93	147.3 \pm 15.7	160.6 \pm 16.9	219.4 \pm 28.1	336.5 \pm 36.2	1.45 \pm 0.05	...
MIPS15999	17:19:35.0+59:42:41.3	..., 1462, 1706	22.27	34.5 \pm 5.1 ^{e,d,i}	40.9 \pm 5.9	53.6 \pm 7.6 ^e	83.0 \pm 16.1	1.37 \pm 0.03	...
MIPS16037	17:21:33.9+59:50:46.9	483, 1462, 1706	24.31	89.9 \pm 9.5	214.6 \pm 22.7	388.5 \pm 42.3	711.6 \pm 73.8	1.26 \pm 0.06	2.16 \pm 0.30
MIPS16047	17:23:01.4+59:40:54.0	483, 1462, 1706	20.95	164.1 \pm 17.1	167.9 \pm 18.1	209.6 \pm 26.2	275.3 \pm 32.3	1.29 \pm 0.06	2.68 \pm 0.85
MIPS16066	17:21:23.7+59:56:17.4	483, 1462, 1706	21.99 ^{a,c}	185.1 \pm 19.6	171.0 \pm 17.9	211.7 \pm 28.0	515.1 \pm 54.8	1.30 \pm 0.06	...
MIPS16099	17:19:37.5+60:01:24.9	483, 1462, 1706	23.11	74.2 \pm 8.4	129.7 \pm 14.5	225.7 \pm 28.8	421.1 \pm 45.8	1.24 \pm 0.06	...
MIPS16118	17:22:16.3+59:47:00.8	..., 1462, 1706	...	52.3 \pm 6.8	35.6 \pm 5.1	<35.9 ^g	146.4 \pm 19.8	1.14 \pm 0.06	2.70 \pm 0.77
MIPS16126	17:22:27.5+60:04:30.8	..., 1462, 1706	22.20 ^a	28.9 \pm 4.3	38.2 \pm 5.5	66.2 \pm 15.4	170.1 \pm 22.2	1.09 \pm 0.06	...
MIPS16132	17:21:08.3+59:54:16.0	483, 1462, 1706	22.00	164.3 \pm 10.4 ^{d,i}	222.3 \pm 23.5	338.8 \pm 38.0	502.3 \pm 53.6	1.16 \pm 0.06	...
MIPS16134	17:20:46.7+59:37:42.7	..., 1462, 1706	23.44	28.5 \pm 4.2	52.1 \pm 6.1	101.3 \pm 18.7	239.6 \pm 26.8	1.17 \pm 0.05	...
MIPS16135	17:22:10.0+59:40:05.5	..., 1462, 1706	22.51	53.9 \pm 17.3 ^{d,i}	60.9 \pm 11.9 ^{d,i}	96.4 \pm 17.7	174.4 \pm 22.2	1.21 \pm 0.06	...
MIPS16152	17:20:55.8+59:35:41.8	..., 1462, 1706	23.01	44.2 \pm 5.6 ^{d,i}	70.4 \pm 10.8 ^{d,i}	99.9 \pm 17.8	264.5 \pm 30.8	1.12 \pm 0.06	...
MIPS16156	17:22:56.8+59:30:58.7	..., 1462, 1706	21.47 ^b	128.3 \pm 36.0 ^{d,i}	101.5 \pm 22.4 ^{d,i}	61.8 \pm 15.1	135.6 \pm 18.6	1.16 \pm 0.06	3.68 \pm 0.18
MIPS16170	17:22:33.3+60:15:14.4	..., 1462, 1706	20.52	99.3 \pm 10.9	91.6 \pm 10.8	<41.7 ^g	225.1 \pm 27.4	1.09 \pm 0.06	1.77 \pm 0.63
MIPS16202	17:22:02.1+59:32:55.6	483, 1462, 1706	22.64	66.9 \pm 8.1	94.5 \pm 10.7	162.8 \pm 22.0	281.6 \pm 32.9	1.02 \pm 0.06	...
MIPS16206	17:21:10.4+60:06:08.2	..., 1462, 1706	...	94.5 \pm 10.4 ^d	147.7 \pm 15.7 ^d	82.1 \pm 15.4	112.3 \pm 15.9	0.98 \pm 0.06 ^d	...
MIPS16219	17:20:13.2+60:10:28.3	483, 1462, 1706	22.88	58.4 \pm 6.9	110.5 \pm 12.3	165.7 \pm 23.5	315.1 \pm 36.0	1.03 \pm 0.06	...
MIPS16227	17:19:20.2+60:14:48.7	..., 1462, 1706	23.92	40.3 \pm 5.1	63.3 \pm 7.8	109.4 \pm 18.9	233.0 \pm 28.0	1.06 \pm 0.06	...
MIPS16249	17:22:08.4+59:45:54.4	..., 1462, 1706	20.47	54.3 \pm 5.9	60.7 \pm 7.3	36.7 \pm 9.6	132.4 \pm 17.9	0.99 \pm 0.06	2.14 \pm 0.33
MIPS16267	17:19:10.3+60:13:16.0	483, 1462, 1706	24.36	47.9 \pm 5.6	93.4 \pm 11.0	155.0 \pm 20.1	283.6 \pm 33.3	1.04 \pm 0.06	1.56 \pm 0.37
MIPS22196	17:22:45.2+59:03:28.3	483, 487, 487	21.00	215.8 \pm 19.6 ^{d,i}	358.9 \pm 29.9 ^{d,i}	618.3 \pm 66.1	1041.1 \pm 106.5	4.73 \pm 0.06	...
MIPS22235	17:20:17.2+59:16:37.4	483, 731, 975	20.57 ^b	583.6 \pm 58.8 ^d	401.2 \pm 41.0 ^d	281.5 \pm 32.6	299.6 \pm 33.1 ^d	3.16 \pm 0.07 ^d	...
MIPS22248	17:20:03.6+59:19:08.0	483, 731, 975	21.98	114.4 \pm 12.4	180.5 \pm 19.1	321.2 \pm 38.1	609.7 \pm 64.9	2.98 \pm 0.07	...
MIPS22307	17:19:51.4+58:42:22.8	483, 975, 1218	20.50	171.9 \pm 17.7	197.7 \pm 21.0	254.9 \pm 29.5	403.6 \pm 44.1	2.02 \pm 0.06	2.14 \pm 0.08
MIPS22323	17:22:34.1+59:10:01.7	483, 731, 975	21.60	251.7 \pm 25.9	230.8 \pm 24.3	238.6 \pm 28.8	403.7 \pm 44.2	1.93 \pm 0.07	...
MIPS22352	17:21:47.7+58:53:55.9	483, 1462, 1706	20.52	228.8 \pm 23.8	218.5 \pm 22.6	229.5 \pm 30.8	294.4 \pm 32.7	1.72 \pm 0.06	2.91 \pm 0.35
MIPS22356	17:20:14.6+59:14:43.6	483, 1462, 1706	23.37	110.8 \pm 12.2	127.3 \pm 13.9	200.7 \pm 26.5	334.0 \pm 37.1	1.69 \pm 0.06	...
MIPS22371	17:23:00.5+59:11:07.9	483, 1462, 1706	...	72.4 \pm 8.4	115.9 \pm 12.8	173.9 \pm 23.8	340.7 \pm 37.1	1.64 \pm 0.06	2.84 \pm 0.05
MIPS22379	17:19:18.6+59:00:42.6	483, 1462, 1706	20.87	227.3 \pm 23.4	176.6 \pm 18.4	256.7 \pm 29.9	358.0 \pm 38.3	1.58 \pm 0.06	3.29 \pm 0.11
MIPS22397	17:20:06.0+59:17:45.3	483, 1462, 1706	23.12	99.5 \pm 11.1	169.9 \pm 17.7	284.4 \pm 35.0	489.7 \pm 50.7	1.57 \pm 0.06	...
MIPS22417	17:23:01.6+59:15:01.5	483, 1462, 1706	22.36	57.8 \pm 6.4	86.9 \pm 9.5	162.5 \pm 20.5	296.8 \pm 31.9	1.52 \pm 0.06	...
MIPS22424	17:21:36.9+59:16:07.8	483, 1462, 1706	21.80 ^{a,c}	84.8 \pm 9.5	146.6 \pm 16.0	261.1 \pm 32.3	500.2 \pm 53.3	1.44 \pm 0.06	4.00 \pm 0.19
MIPS22516	17:21:33.7+59:07:28.1	..., 1462, 1706	22.26	67.7 \pm 8.1 ^h	69.0 \pm 8.1 ^h	67.0 \pm 15.5	97.2 \pm 14.4	1.32 \pm 0.06	...
MIPS22527	17:18:15.5+59:12:00.7	483, 1462, 1706	22.87 ^{b,c}	90.9 \pm 9.7	139.7 \pm 14.5	259.9 \pm 29.9	433.3 \pm 44.5	1.24 \pm 0.06	...
MIPS22536	17:21:08.3+59:01:16.0	..., 1462, 1706	...	109.6 \pm 11.6	157.7 \pm 16.9	69.5 \pm 12.5	115.1 \pm 15.6	1.28 \pm 0.06	...
MIPS22548	17:23:30.5+58:44:48.8	..., 1462, 1706	...	9.2 \pm 2.8	36.6 \pm 5.4	45.8 \pm 13.0	228.7 \pm 27.4	1.28 \pm 0.06	...
MIPS22549	17:22:13.9+59:17:40.5	483, 1462, 1706	23.64	81.6 \pm 8.8	134.2 \pm 14.8	232.0 \pm 27.9	427.8 \pm 46.4	1.17 \pm 0.06	2.30 \pm 0.01
MIPS22555	17:21:31.0+58:42:49.0	..., 1462, 1706	23.71 ^{a,c}	78.4 \pm 9.1 ^h	104.8 \pm 12.1 ^h	152.3 \pm 22.0 ^h	194.1 \pm 25.7 ^h	1.19 \pm 0.06 ^h	...
MIPS22557	17:20:25.5+59:13:59.1	..., 1462, 1706	20.88	128.8 \pm 13.5	86.1 \pm 9.9	63.2 \pm 12.6	87.4 \pm 16.0	1.12 \pm 0.06	3.37 \pm 0.20

^hTwo or more sources that could be at similar redshifts are comprised in the IRAC or MIPS flux.

ⁱTo recover the flux of this source, we first deblended it from its neighbour(s) using point-spread-funtion fitting that was carried out with galfit. Once the best fitting parameters were determined, we removed the neighbour(s) and measured the flux of the source using SExtractor, as for all other sources.

^jThis source is blended with a star. Its flux cannot be recovered.

TABLE 2

REDSHIFT, ABSORPTION STRENGTH, AND REST-FRAME 14 μm MONOCHROMATIC LUMINOSITY MEASUREMENTS.

Galaxy (1)	z (2)	confidence (3)	emission lines or features (4)	absorption feature (5)	$\tau_{9.7\mu\text{m}}$ (6)	νL_ν (14 μm) (7)
MIPS34	1.38±0.03	a	PAH 6.2,PAH 7.7,PAH 8.6,[NeII]	silicate	0.14	2.08×10^{12}
MIPS39	2.42	c	PAH 8.6	silicate (partial)	0.87	...
MIPS55	0.80±0.03	a	PAH 11.3,PAH 12.7	silicate	0.48	4.34×10^{11}
MIPS159
MIPS168	0.24±0.01	a	PAH 7.7,PAH 11.3,PAH 12.7,PAH 17.0	silicate	0.74	6.31×10^9
MIPS184
MIPS213	1.22	b	PAH 6.2	silicate	0.20	5.75×10^{11}
MIPS224	1.47±0.02	a	PAH 6.2,PAH 7.7,PAH 8.6,PAH 12.7	...	0.00	...
MIPS268	1.69	b	PAH 7.7	silicate	0.67	...
MIPS277	1.06±0.02	a	PAH 7.7,PAH 11.3,PAH 12.7	...	0.00	2.58×10^{11}
MIPS298	3.49	b	PAH 6.2	silicate	3.54	...
MIPS322
MIPS324	0.96±0.01	a	PAH 6.2,PAH 7.7,PAH 11.3,PAH 12.7,[NeIII]	silicate	0.19	1.59×10^{11}
MIPS331	1.03	d,f	...	silicate
MIPS350	0.94±0.02	a	PAH 8.6,PAH 11.3,PAH 12.7,[NeIII]	silicate	0.45	2.20×10^{11}
MIPS351
MIPS358	0.81±0.02	a	PAH 11.3,PAH 12.7	silicate	0.02	6.00×10^{10}
MIPS369	3.21	e,f	PAH 6.2	silicate (partial)
MIPS394	0.92±0.01	a	PAH 11.3,PAH 12.7	silicate	1.08	1.11×10^{11}
MIPS397	1.35	b	...	silicate	0.12	4.58×10^{11}
MIPS419	0.83	c	...	silicate	2.60	1.40×10^{11}
MIPS446	0.82±0.01	d	PAH 8.6,PAH 12.7,[NeIII]
MIPS463	2.44	e	PAH 6.2
MIPS472	0.92±0.02	a	PAH 11.3,PAH 12.7	1.22×10^{11}
MIPS488	0.69±0.02	a	PAH 11.3,PAH 12.7,PAH 17.0	silicate	0.81	6.00×10^{10}
MIPS495
MIPS505
MIPS509	≥2.28	f	...	silicate (partial)
MIPS512	0.99±0.01	a	PAH 12.7,[NeIII]	silicate	0.84	1.84×10^{11}
MIPS521	2.06±0.01	a	PAH 6.2,PAH 7.7,PAH 8.6	...	0.24	...
MIPS530	0.89±0.02	a	PAH 11.3,PAH 12.7	silicate	1.32	6.89×10^{10}
MIPS532	1.54	b	...	silicate	1.51	...
MIPS537	0.39±0.01	a	PAH 6.2,PAH 7.7,PAH 11.3,PAH 12.7,[NeIII],PAH 17.0	silicate	0.32	1.13×10^{10}
MIPS542	0.91±0.01	a	PAH 11.3,PAH 12.7	silicate	0.09	1.06×10^{11}
MIPS544	0.96	b	...	silicate	1.12	1.62×10^{11}
MIPS546	1.07±0.01	a	PAH 7.7,PAH 11.3,PAH 12.7	silicate	0.47	2.21×10^{11}
MIPS549	0.93±0.01	a	PAH 11.3,PAH 12.7,PAH 17.0	...	0.00	5.87×10^{10}
MIPS562	0.54±0.01	a	PAH 6.2,PAH 7.7,PAH 11.3,PAH 12.7	silicate	1.06	4.21×10^{10}
MIPS7985
MIPS8040	0.76±0.01	a	PAH 6.2,PAH 7.7,PAH 11.3,PAH 12.7,PAH 17.0	silicate	1.73	2.12×10^{11}
MIPS8069	1.45	e	...	silicate	0.28	...
MIPS8071	0.98	d	PAH 12.7
MIPS8098	1.07	d	PAH 6.2,PAH 12.7
MIPS8107	0.94±0.03	a	PAH 7.7,PAH 11.3,[NeIII]	silicate	0.33	3.36×10^{11}
MIPS8121	1.21±0.03	a	PAH 6.2,PAH 7.7	silicate	0.25	8.00×10^{11}
MIPS8157
MIPS8172	1.11±0.03	d	PAH 6.2,PAH 11.3
MIPS8179	0.59±0.01	a	PAH 11.3,PAH 12.7,[NeIII]	silicate	0.55	7.62×10^{10}
MIPS8185
MIPS8192
MIPS8204	0.84±0.02	a	PAH 11.3,PAH 12.7	1.49×10^{11}
MIPS8224
MIPS8226	2.10	c	PAH 7.7	silicate	0.41	...
MIPS8233
MIPS8251	1.94	b	PAH 7.7	silicate	0.59	...
MIPS8253	0.96±0.01	a	PAH 7.7,PAH 11.3,PAH 12.7,[NeIII]	silicate	2.03	2.18×10^{11}
MIPS8308	0.37±0.01	a	PAH 11.3,PAH 12.7	6.41×10^9
MIPS8311	1.18±0.01	a	PAH 7.7,PAH 11.3,PAH 12.7	silicate	1.13	3.09×10^{11}
MIPS8315
MIPS8325	0.61±0.02	a	PAH 11.3,PAH 12.7,[NeIII]	silicate	1.14	6.91×10^{10}
MIPS8328	1.02	b	PAH 11.3	silicate	0.26	1.83×10^{11}
MIPS8360	1.50±0.02	a	PAH 6.2,PAH 7.7,PAH 11.3,PAH 12.7	silicate	0.57	...
MIPS8371	0.35±0.01	a	PAH 6.2,PAH 7.7,PAH 11.3,PAH 12.7,PAH 17.0	silicate	0.43	9.24×10^9
MIPS8375	0.87±0.01	a	PAH 11.3,PAH 12.7,[NeIII]	silicate	0.92	1.15×10^{11}
MIPS8377	0.84±0.01	a	PAH 11.3,PAH 12.7,[NeIII]	silicate	1.67	1.17×10^{11}
MIPS8384	0.92±0.01	a	PAH 6.2,PAH 7.7,PAH 11.3,PAH 12.7,[NeIII]	silicate	0.01	1.87×10^{11}
MIPS8387	0.92±0.01	a	PAH 11.3,PAH 12.7	...	0.00	6.60×10^{10}
MIPS8388	1.14±0.02	a	PAH 11.3,PAH 12.7	silicate	0.11	2.53×10^{11}
MIPS8392	1.90	b	...	silicate	4.56	...
MIPS8400
MIPS8401	0.57±0.01	a	PAH 11.3,PAH 12.7	silicate	0.52	4.77×10^{10}
MIPS8405	1.17±0.01	a	PAH 7.7,PAH 11.3,PAH 12.7	...	0.00	3.36×10^{11}
MIPS8407
MIPS8407
MIPS8409	0.74±0.04	d	PAH 12.7,PAH 17.0
MIPS8411	2.06	c	PAH 7.7	silicate	0.26	...
MIPS8413	2.18	d,f	PAH 6.2	silicate
MIPS8424	1.59	b	PAH 12.7	silicate	0.20	...
MIPS8430	0.67±0.01	a	PAH 11.3,PAH 12.7,[NeIII]	silicate	1.15	4.59×10^{10}
MIPS8450	1.01±0.01	a	PAH 7.7,PAH 11.3,PAH 12.7	...	0.00	8.67×10^{10}
MIPS8462	1.01±0.02	a	PAH 11.3,PAH 12.7	silicate	0.19	2.11×10^{11}
MIPS8465
MIPS8477	1.84±0.01	a	PAH 7.7,PAH 11.3	silicate	0.41	...
MIPS8479	1.30	b	...	silicate	2.36	1.31×10^{12}
MIPS8495	1.28	b	PAH 8.6	silicate	0.08	3.26×10^{11}
MIPS8499	0.60±0.02	a	PAH 11.3,PAH 12.7	5.10×10^{10}

TABLE 2—Continued

Galaxy (1)	z (2)	confidence (3)	emission lines or features (4)	absorption feature (5)	$\tau_{9.7\mu\text{m}}$ (6)	$\nu L_\nu(14\ \mu\text{m})$ (7)
MIPS8507	0.76±0.02	a	PAH 11.3,PAH 12.7,PAH 17.0	silicate	0.75	5.69×10^{10}
MIPS8521	1.19±0.02	a	PAH 7.7,PAH 12.7	silicate	1.90	5.02×10^{11}
MIPS8526	0.84	b,g	PAH 12.7	silicate	1.36	7.98×10^{10}
MIPS8532	0.86±0.01	a	PAH 11.3,PAH 12.7, [NeIII]	silicate	0.59	1.08×10^{11}
MIPS8543	0.65±0.01	a	PAH 11.3,PAH 12.7	silicate	0.34	8.94×10^{10}
MIPS8550	0.87	b	...	silicate	2.24	1.24×10^{11}
MIPS15678	1.37	d	PAH 6.2,PAH 11.3,PAH 12.7
MIPS15690	0.85	b	PAH 12.7	silicate	0.04	6.79×10^{11}
MIPS15755	0.73±0.02	a	PAH 6.2,PAH 7.7,PAH 11.3,PAH 12.7, [NeIII],PAH 17.0	...	0.00	2.27×10^{11}
MIPS15771	1.32	d,e,f	...	silicate
MIPS15776	1.12	b	PAH 12.7	silicate	0.48	6.63×10^{11}
MIPS15796	1.45	f	...	silicate
MIPS15871
MIPS15897	1.62	d	PAH 11.3,PAH 12.7
MIPS15941	1.23	e,f	...	silicate
MIPS15967
MIPS15997	0.57±0.01	a	PAH 12.7, [NeIII]	silicate	0.76	6.16×10^{10}
MIPS16037	1.64	b	PAH 12.7	silicate	1.04	...
MIPS16047	0.52±0.02	a	PAH 7.7, [NeIII]	silicate	1.13	4.55×10^{10}
MIPS16066	1.00	b	PAH 7.7	silicate	0.87	3.13×10^{11}
MIPS16099	0.95	d	[NeIII]	silicate
MIPS16118	2.61	c	PAH 6.2	silicate (partial)
MIPS16126
MIPS16132
MIPS16134	1.20	d	PAH 12.7	silicate
MIPS16135	0.62	d	PAH 12.7
MIPS16152	1.83	c	PAH 7.7	silicate	1.19	...
MIPS16156	0.72	b	[NeIII]	silicate	0.48	6.70×10^{10}
MIPS16170	0.32±0.01	a	PAH 11.3,PAH 12.7	1.07×10^{10}
MIPS16202
MIPS16206	0.87±0.02	a	PAH 11.3,PAH 12.7, [NeIII]	silicate	0.49	1.14×10^{11}
MIPS16219
MIPS16227	2.15	e	PAH 7.7
MIPS16249	0.53±0.02	a	PAH 11.3,PAH 12.7	3.37×10^{10}
MIPS16267	1.31	b	PAH 12.7	silicate	0.61	5.57×10^{11}
MIPS22196
MIPS22235	0.42±0.01	a	PAH 7.7,PAH 8.6,PAH 11.3,PAH 12.7	silicate	0.55	8.33×10^{10}
MIPS22248
MIPS22307	0.70±0.01	a	PAH 6.2,PAH 7.7,PAH 8.6,PAH 11.3	...	0.00	1.33×10^{11}
MIPS22323	1.21±0.01	a	PAH 6.2,PAH 7.7,PAH 12.7	silicate	0.10	5.28×10^{11}
MIPS22352	0.66±0.01	a	PAH 6.2,PAH 7.7,PAH 11.3,PAH 12.7	silicate	0.19	7.61×10^{10}
MIPS22356	1.13±0.01	a	PAH 8.6,PAH 11.3,PAH 12.7	silicate	0.39	6.22×10^{11}
MIPS22371	1.67±0.01	a	PAH 6.2,PAH 7.7,PAH 11.3	silicate	0.37	...
MIPS22379	0.65±0.02	a	PAH 8.6,PAH 11.3	silicate	0.13	8.55×10^{10}
MIPS22397
MIPS22417	1.96±0.02	a	PAH 6.2,PAH 8.6,PAH 11.3	silicate (partial)	0.90	...
MIPS22432	1.59±0.01	a	PAH 6.2,PAH 11.3,PAH 12.7	silicate	1.18	...
MIPS22516	1.35	e	PAH 7.7
MIPS22527
MIPS22536	1.59±0.02	b	PAH 6.2,PAH 11.3	silicate	0.51	...
MIPS22548	≥2.12	f	...	silicate (partial)
MIPS22549	1.05±0.01	a	PAH 11.3,PAH 12.7	silicate	0.01	2.46×10^{11}
MIPS22555	1.88	b	...	silicate	0.08	...
MIPS22557	0.78±0.01	a	PAH 11.3,PAH 12.7, [NeIII]	silicate	...	9.36×10^{10}
MIPS22621	0.59	e	PAH 12.7
MIPS22633	2.20	e	PAH 6.2
MIPS22634
MIPS22635	0.80±0.01	a	PAH 11.3,PAH 12.7	silicate	0.78	1.25×10^{11}
MIPS22638	0.99	b	[NeII]	silicate	0.39	1.72×10^{11}
MIPS22663
MIPS22690	2.07	b	...	silicate	0.39	...
MIPS22710
MIPS22722	1.71	b	PAH 8.6	silicate	0.55	...
MIPS22725
MIPS22744

NOTE.—Column (2): Redshifts based on MIR spectra. Uncertainties are given for all sources that have more than two 3σ detected emission lines or features. For all other sources, the plausible redshift uncertainty is in the range [0.01,0.3].

Column (3): Classification of the confidence of the MIR redshift. The letters correspond to:

a: The redshift is confirmed by more than two emission lines or features that have $> 3\sigma$ detections.

b: The redshift is either derived from a single emission line but confirmed from the 9.7 μm silicate absorption feature or measured from the silicate absorption feature. The uncertainty in this redshift measurement is typically of order 0.1, but it can be as high as 0.3.

c: The redshift is measured from a single emission line and confirmed by the presence of part of the 9.7 μm silicate feature in the spectrum. The accuracy of the measurement can be lower than that of category (b).

d: More than one solutions are possible. This redshift is uncertain.

e: Only one line or feature had a significant detection. This redshift is also uncertain.

f: Only part of the 9.7 μm silicate absorption feature was seen in the MIPS spectral range, or the silicate feature had a very small optical depth, < 0.1 . This redshift is uncertain.

g: This spectrum contains features of two spatially unresolved sources, one at $z=0.84$, and a somewhat fainter at $z=0.91$. This could either be a binary merging system, or sources that neighbour each other due to projection effects.

Column (4): Emission lines or dust features used for the computation of each source's redshift. These features have a signal-to-noise ratio greater than 3 when fitted with a Lorentzian profile. Unless otherwise noted, the 12.7 complex refers to the blended 12.6 and 12.7 μm dust features and the [NeII] line.

Column (5): Indicates whether the 9.7 μm silicate absorption feature was used in the redshift computation. Partially detected silicate absorption features were not used for that purpose.

Column (6): The 9.7 μm silicate feature optical depth was measured with PAHFIT for sources with reliable redshifts, i.e. with confidence classification a,b, or c in column 3.

Column (7): The rest-frame monochromatic 14 μm luminosity is given in units of solar luminosity for sources with reliable redshift measurements.

TABLE 3

FLUXES AND EWs OF EMISSION LINES OR FEATURES IN THE RANGE $6.0 < \lambda < 11.0 \mu\text{m}$.

Galaxy (MIPS)	$f_{6.2}$ (Wcm $^{-2}$)	$EW_{6.2}$ (μm)	$f_{7.7}$ (Wcm $^{-2}$)	$EW_{7.7}$ (μm)	$f_{8.6}$ (Wcm $^{-2}$)	$EW_{8.6}$ (μm)	$f_{[SIV]}$ (Wcm $^{-2}$)	$EW_{[SIV]}$ (μm)
MIPS34	$6.65(\pm 1.13) \times 10^{-22}$	0.07 ± 0.01	$3.71(\pm 0.41) \times 10^{-21}$	0.42 ± 0.05	$< 3.31 \times 10^{-22}$...	$< 5.19 \times 10^{-23}$...
MIPS39	$3.02(\pm 0.67) \times 10^{-22}$	0.03 ± 0.01	$2.85(\pm 0.19) \times 10^{-21}$	0.42 ± 0.03
MIPS55	$7.40(\pm 1.47) \times 10^{-22}$	0.22 ± 0.04	$1.99(\pm 0.46) \times 10^{-22}$	0.06 ± 0.01
MIPS168	$4.73(\pm 0.43) \times 10^{-21}$	9.70 ± 0.88	$8.10(\pm 1.61) \times 10^{-22}$	1.83 ± 0.36	$< 1.27 \times 10^{-22}$...
MIPS213	$< 3.98 \times 10^{-22}$...	$< 6.22 \times 10^{-22}$...	$< 2.59 \times 10^{-22}$...	$< 4.24 \times 10^{-23}$...
MIPS224	$5.30(\pm 0.57) \times 10^{-22}$	0.33 ± 0.04	$1.53(\pm 0.19) \times 10^{-21}$	0.92 ± 0.11	$5.01(\pm 0.79) \times 10^{-22}$	0.29 ± 0.05	$5.20(\pm 1.19) \times 10^{-23}$	0.03 ± 0.01
MIPS268	$2.82(\pm 0.80) \times 10^{-22}$	0.09 ± 0.03	$1.60(\pm 0.26) \times 10^{-21}$	0.64 ± 0.10	$< 1.04 \times 10^{-22}$...	$7.73(\pm 1.17) \times 10^{-23}$	0.06 ± 0.01
MIPS277	$1.91(\pm 0.16) \times 10^{-21}$	1.20 ± 0.10	$5.67(\pm 1.08) \times 10^{-22}$	0.38 ± 0.07	$< 6.15 \times 10^{-23}$...
MIPS298	$2.07(\pm 0.45) \times 10^{-22}$	0.11 ± 0.02	$< 2.15 \times 10^{-21}$
MIPS324	$5.41(\pm 1.11) \times 10^{-22}$	0.35 ± 0.07	$1.81(\pm 0.16) \times 10^{-21}$	1.40 ± 0.12	$4.01(\pm 1.00) \times 10^{-22}$	0.35 ± 0.09	$< 1.16 \times 10^{-22}$...
MIPS350	$1.18(\pm 0.11) \times 10^{-21}$	2.88 ± 0.27	$< 1.34 \times 10^{-22}$
MIPS358	$< 8.97 \times 10^{-23}$...
MIPS394	$< 1.31 \times 10^{-22}$...
MIPS397	$3.17(\pm 0.90) \times 10^{-22}$	0.17 ± 0.05	$1.45(\pm 0.26) \times 10^{-21}$	0.97 ± 0.17	$< 3.74 \times 10^{-22}$...	$< 3.60 \times 10^{-23}$...
MIPS419	$< 6.81 \times 10^{-22}$...
MIPS472	$< 1.09 \times 10^{-22}$...
MIPS488	$< 1.87 \times 10^{-22}$...
MIPS512	$< 2.96 \times 10^{-22}$...	$< 9.35 \times 10^{-22}$...	$< 3.95 \times 10^{-22}$...	$< 1.41 \times 10^{-22}$...
MIPS521	$5.87(\pm 1.04) \times 10^{-22}$	0.69 ± 0.12	$1.87(\pm 0.28) \times 10^{-21}$	2.97 ± 0.44	$3.69(\pm 0.52) \times 10^{-22}$	0.75 ± 0.11	$1.12(\pm 0.17) \times 10^{-22}$	0.35 ± 0.05
MIPS530	$< 1.18 \times 10^{-22}$...
MIPS532	$< 2.91 \times 10^{-22}$...	$4.85(\pm 0.33) \times 10^{-21}$	2.34 ± 0.16	$< 2.17 \times 10^{-22}$...	$< 5.54 \times 10^{-23}$...
MIPS537	$1.14(\pm 0.10) \times 10^{-21}$	1.89 ± 0.17	$3.66(\pm 0.29) \times 10^{-21}$	7.31 ± 0.58	$1.01(\pm 0.12) \times 10^{-21}$	2.56 ± 0.30	$< 1.06 \times 10^{-22}$...
MIPS542	$< 1.17 \times 10^{-22}$...
MIPS544	$< 5.55 \times 10^{-22}$...	$< 2.00 \times 10^{-22}$...
MIPS546	$5.69(\pm 0.32) \times 10^{-21}$	19.26 ± 1.08	$1.36(\pm 0.12) \times 10^{-21}$	4.44 ± 0.39	$< 7.52 \times 10^{-23}$
MIPS549	$5.94(\pm 1.11) \times 10^{-22}$	1.19 ± 0.22	$< 1.33 \times 10^{-22}$
MIPS562	$1.72(\pm 0.12) \times 10^{-21}$	2.23 ± 0.16	$5.96(\pm 0.41) \times 10^{-21}$	7.25 ± 0.50	$5.09(\pm 1.67) \times 10^{-22}$	0.78 ± 0.26	$< 2.00 \times 10^{-22}$...
MIPS840	$1.74(\pm 0.09) \times 10^{-21}$	0.64 ± 0.03	$5.70(\pm 0.47) \times 10^{-21}$	2.30 ± 0.19	$1.80(\pm 0.13) \times 10^{-21}$	1.06 ± 0.08	$9.95(\pm 3.01) \times 10^{-23}$	0.09 ± 0.03
MIPS8107	$< 4.51 \times 10^{-22}$...	$1.99(\pm 0.45) \times 10^{-21}$	1.06 ± 0.24	$3.15(\pm 0.91) \times 10^{-22}$	0.21 ± 0.06	$< 1.21 \times 10^{-22}$...
MIPS8121	$2.88(\pm 0.75) \times 10^{-22}$	0.10 ± 0.03	$2.00(\pm 0.24) \times 10^{-21}$	0.77 ± 0.09	$< 3.44 \times 10^{-22}$...	$< 4.77 \times 10^{-23}$...
MIPS8179	$< 2.53 \times 10^{-22}$...	$< 3.70 \times 10^{-22}$...	$< 4.37 \times 10^{-22}$...	$< 1.11 \times 10^{-22}$...
MIPS8204	$< 1.32 \times 10^{-22}$...
MIPSS226	$< 2.96 \times 10^{-22}$...	$1.07(\pm 0.26) \times 10^{-21}$	0.69 ± 0.17	$< 2.04 \times 10^{-22}$...	$< 7.47 \times 10^{-23}$...
MIPSS251	$< 3.16 \times 10^{-22}$...	$1.14(\pm 0.08) \times 10^{-21}$	0.72 ± 0.05	$2.22(\pm 0.52) \times 10^{-22}$	0.17 ± 0.04	$< 6.60 \times 10^{-23}$...
MIPSS253	$1.92(\pm 0.10) \times 10^{-22}$	$0.07 \pm 0.00^*$	$2.48(\pm 0.08) \times 10^{-21}$	1.39 ± 0.04	$4.51(\pm 0.87) \times 10^{-22}$	0.46 ± 0.09	$3.82(\pm 1.07) \times 10^{-23}$	0.08 ± 0.02
MIPSS308
MIPSS311	$1.77(\pm 0.12) \times 10^{-21}$	1.27 ± 0.09	$< 5.81 \times 10^{-22}$...	$< 5.89 \times 10^{-23}$...
MIPSS325	$< 1.80 \times 10^{-22}$...
MIPSS328	$< 4.08 \times 10^{-22}$...	$< 9.84 \times 10^{-23}$...
MIPSS360	$6.03(\pm 1.01) \times 10^{-22}$	0.45 ± 0.08	$1.42(\pm 0.34) \times 10^{-21}$	0.96 ± 0.23	$3.68(\pm 0.86) \times 10^{-22}$	0.26 ± 0.06	$4.42(\pm 1.18) \times 10^{-23}$	0.03 ± 0.01
MIPSS371	$1.59(\pm 0.12) \times 10^{-21}$	2.09 ± 0.16	$5.32(\pm 0.37) \times 10^{-21}$	9.81 ± 0.68	$1.10(\pm 0.12) \times 10^{-21}$	2.69 ± 0.29	$< 1.25 \times 10^{-22}$...
MIPSS375	$1.44(\pm 0.32) \times 10^{-22}$	0.38 ± 0.09
MIPSS377	$1.60(\pm 0.37) \times 10^{-22}$	0.67 ± 0.16
MIPSS384	$< 3.40 \times 10^{-22}$...	$2.20(\pm 0.12) \times 10^{-21}$	1.98 ± 0.11	$< 2.91 \times 10^{-22}$...	$< 9.87 \times 10^{-23}$...
MIPSS387
MIPSS388	$2.29(\pm 0.39) \times 10^{-21}$	2.18 ± 0.37	$6.72(\pm 1.25) \times 10^{-22}$	0.84 ± 0.16	$< 6.45 \times 10^{-23}$...
MIPSS392	$< 1.21 \times 10^{-21}$...	$2.73(\pm 0.42) \times 10^{-21}$	1.91 ± 0.29	$< 1.22 \times 10^{-22}$...	$< 1.44 \times 10^{-21}$...
MIPSS401	$< 1.21 \times 10^{-22}$...
MIPSS405	$3.92(\pm 0.29) \times 10^{-21}$	8.01 ± 0.59	$9.81(\pm 1.17) \times 10^{-22}$	1.63 ± 0.19	$< 5.19 \times 10^{-23}$...
MIPSS411	$2.78(\pm 0.73) \times 10^{-22}$	0.19 ± 0.05	$7.23(\pm 1.82) \times 10^{-21}$	0.62 ± 0.16	$1.27(\pm 0.42) \times 10^{-22}$	0.12 ± 0.04
MIPSS424	$< 2.58 \times 10^{-22}$...	$1.62(\pm 0.26) \times 10^{-21}$	1.61 ± 0.26	$2.01(\pm 0.66) \times 10^{-22}$	0.20 ± 0.06	$< 3.96 \times 10^{-23}$...
MIPSS430	$< 9.78 \times 10^{-23}$...
MIPSS450	$4.97(\pm 0.28) \times 10^{-21}$	7.11 ± 0.40	$1.08(\pm 0.11) \times 10^{-21}$	2.07 ± 0.21	$< 7.08 \times 10^{-23}$...
MIPSS462	$1.98(\pm 0.60) \times 10^{-21}$	4.49 ± 1.36	$3.64(\pm 1.16) \times 10^{-22}$	0.75 ± 0.24	$< 7.62 \times 10^{-23}$...
MIPSS477	$3.63(\pm 0.86) \times 10^{-22}$	0.35 ± 0.08	$1.09(\pm 0.33) \times 10^{-21}$	1.19 ± 0.36	$< 1.86 \times 10^{-22}$...	$4.64(\pm 1.12) \times 10^{-23}$	0.06 ± 0.02
MIPSS479	$< 1.25 \times 10^{-21}$...	$< 5.57 \times 10^{-23}$...
MIPSS495	$< 2.21 \times 10^{-22}$...	$1.49(\pm 0.23) \times 10^{-21}$	1.00 ± 0.15	$< 3.04 \times 10^{-22}$...	$7.15(\pm 1.36) \times 10^{-23}$	0.06 ± 0.01
MIPSS499	$< 1.01 \times 10^{-22}$...
MIPSS507	$< 1.04 \times 10^{-22}$...
MIPSS521	$< 6.27 \times 10^{-22}$...	$4.30(\pm 0.29) \times 10^{-21}$	1.86 ± 0.13	$5.72(\pm 1.04) \times 10^{-22}$	0.43 ± 0.08	$< 5.57 \times 10^{-23}$...
MIPSS526	$< 1.74 \times 10^{-22}$...
MIPSS532	$< 1.33 \times 10^{-22}$...
MIPSS543	$< 1.39 \times 10^{-22}$...
MIPSS550	$< 4.50 \times 10^{-22}$...
MIPSS5690	$< 2.59 \times 10^{-22}$...	$4.21(\pm 0.30) \times 10^{-21}$	0.71 ± 0.05	$< 4.62 \times 10^{-22}$...	$< 1.39 \times 10^{-22}$...
MIPSS5755	$1.89(\pm 0.11) \times 10^{-21}$	0.84 ± 0.05	$6.65(\pm 0.34) \times 10^{-21}$	3.36 ± 0.17	$1.68(\pm 0.15) \times 10^{-21}$	0.87 ± 0.08	$< 1.06 \times 10^{-22}$...
MIPSS5776	$< 3.59 \times 10^{-22}$...	$1.44(\pm 0.29) \times 10^{-21}$	0.35 ± 0.07	$< 3.14 \times 10^{-22}$...	$< 6.02 \times 10^{-23}$...
MIPSS5999	$< 1.19 \times 10^{-22}$...
MIPSS16037	$2.17(\pm 0.70) \times 10^{-22}$	0.05 ± 0.02	$3.14(\pm 0.25) \times 10^{-21}$	1.09 ± 0.09	$< 1.27 \times 10^{-22}$...	$< 6.42 \times 10^{-23}$...
MIPSS16047	$4.93(\pm 1.26) \times 10^{-22}$	0.30 ± 0.08	$2.00(\pm 0.35) \times 10^{-21}$	1.36 ± 0.24	$9.89(\pm 1.18) \times 10^{-22}$	0.90 ± 0.11	$< 1.81 \times 10^{-22}$...
MIPSS16066	$< 3.79 \times 10^{-22}$...	$3.04(\pm 0.30) \times 10^{-21}$	1.76 ± 0.17	$4.11(\pm 0.98) \times 10^{-22}$	0.35 ± 0.08	$< 1.65 \times 10^{-22}$...
MIPSS16118	$< 2.38 \times 10^{-22}$
MIPSS16152	$< 1.27 \times 10^{-21}$...	$2.10(\pm 0.52) \times 10^{-22}$	0.21 ± 0.05	$< 9.93 \times 10^{-23}$...
MIPSS16156	$< 1.16 \times 10^{-22}$...
MIPSS16170
MIPSS16206	$< 1.02 \times 10^{-22}$...
MIPSS16249	$< 8.61 \times 10^{-23}$...

TABLE 3—Continued

Galaxy (MIPS)	$f_{6.2}$ (Wcm $^{-2}$)	$EW_{6.2}$ (μ m)	$f_{7.7}$ (Wcm $^{-2}$)	$EW_{7.7}$ (μ m)	$f_{8.6}$ (Wcm $^{-2}$)	$EW_{8.6}$ (μ m)	$f_{[SIV]}$ (Wcm $^{-2}$)	$EW_{[SIV]}$ (μ m)
MIPS16267	$<3.25 \times 10^{-22}$...	$1.72(\pm 0.35) \times 10^{-21}$	0.76 ± 0.15	$<4.36 \times 10^{-22}$...	$<5.19 \times 10^{-23}$...
MIPS2235	$3.35(\pm 1.11) \times 10^{-22}$	0.43 ± 0.14	$1.83(\pm 0.15) \times 10^{-21}$	2.07 ± 0.17	$8.33(\pm 1.79) \times 10^{-22}$	0.81 ± 0.17	$<1.87 \times 10^{-22}$...
MIPS22307	$1.31(\pm 0.12) \times 10^{-21}$	0.69 ± 0.06	$3.56(\pm 0.44) \times 10^{-21}$	2.07 ± 0.26	$1.28(\pm 0.11) \times 10^{-21}$	0.78 ± 0.07	$<9.21 \times 10^{-23}$...
MIPS22323	$<3.59 \times 10^{-22}$...	$1.43(\pm 0.33) \times 10^{-21}$	0.53 ± 0.12	$<3.98 \times 10^{-22}$...	$<6.41 \times 10^{-23}$...
MIPS22352	$1.92(\pm 0.11) \times 10^{-21}$	2.09 ± 0.12	$7.81(\pm 0.43) \times 10^{-21}$	11.27 ± 0.62	$1.49(\pm 0.12) \times 10^{-21}$	2.35 ± 0.19	$<9.48 \times 10^{-23}$...
MIPS22356	$<4.45 \times 10^{-22}$...	$1.50(\pm 0.46) \times 10^{-21}$	0.78 ± 0.24	$6.44(\pm 1.12) \times 10^{-22}$	0.35 ± 0.06	$<4.46 \times 10^{-23}$...
MIPS22371	$4.37(\pm 0.74) \times 10^{-22}$	0.18 ± 0.03	$1.20(\pm 0.32) \times 10^{-21}$	0.50 ± 0.13	$<1.86 \times 10^{-22}$...	$6.02(\pm 1.10) \times 10^{-23}$	0.03 ± 0.01
MIPS22379	$<3.05 \times 10^{-22}$...	$9.97(\pm 3.14) \times 10^{-22}$	0.80 ± 0.25	$4.59(\pm 1.27) \times 10^{-22}$	0.41 ± 0.11	$<8.73 \times 10^{-23}$...
MIPS22417	$5.02(\pm 0.69) \times 10^{-22}$	0.21 ± 0.03	$1.02(\pm 0.08) \times 10^{-21}$	0.67 ± 0.05	$5.20(\pm 0.48) \times 10^{-22}$	0.55 ± 0.05	$<5.67 \times 10^{-23}$...
MIPS22432	$9.25(\pm 0.80) \times 10^{-22}$	0.26 ± 0.02	$5.50(\pm 0.23) \times 10^{-21}$	2.37 ± 0.10	$8.01(\pm 0.62) \times 10^{-22}$	0.61 ± 0.05	$4.19(\pm 1.06) \times 10^{-23}$	0.06 ± 0.02
MIPS22536	$4.38(\pm 0.91) \times 10^{-22}$	0.27 ± 0.06	$2.55(\pm 0.33) \times 10^{-21}$	1.77 ± 0.23	$5.88(\pm 0.77) \times 10^{-22}$	0.48 ± 0.06	$<5.79 \times 10^{-23}$...
MIPS22549	$<2.20 \times 10^{-22}$...	$1.92(\pm 0.25) \times 10^{-21}$	1.59 ± 0.21	$3.69(\pm 1.04) \times 10^{-22}$	0.35 ± 0.10	$<5.73 \times 10^{-23}$...
MIPS22555	$<8.50 \times 10^{-22}$...	$<1.72 \times 10^{-22}$...	$<4.92 \times 10^{-23}$...
MIPS22557	$<1.21 \times 10^{-22}$...
MIPS22635	$<1.82 \times 10^{-22}$...
MIPS22638	$<4.00 \times 10^{-22}$...	$<1.10 \times 10^{-22}$...
MIPS22690	$<2.62 \times 10^{-22}$...	$4.24(\pm 0.63) \times 10^{-22}$	0.31 ± 0.05	$1.80(\pm 0.45) \times 10^{-22}$	0.18 ± 0.05	$<6.31 \times 10^{-23}$...
MIPS22722	$9.24(\pm 2.61) \times 10^{-22}$	0.71 ± 0.20

NOTE.— Fluxes may not be given for lines that are in the IRS wavelength range when their neighboring continuum cannot be well determined.
* Error bars of 0 correspond to EW uncertainties that are lower than the selected measurement accuracy.

TABLE 4

FLUXES AND EWs OF EMISSION LINES OR FEATURES IN THE RANGE $11.0 < \lambda < 16.0 \mu\text{m}$.

Galaxy (MIPS)	$f_{11.3}$ (Wcm $^{-2}$)	$EW_{11.3}$ (μm)	$f_{12.7}$ (Wcm $^{-2}$)	$EW_{12.7}$ (μm)	$f_{[NeII]}$ (Wcm $^{-2}$)	$EW_{[NeII]}$ (μm)	$f_{[NeIII]}$ (Wcm $^{-2}$)	$EW_{[NeIII]}$ (μm)
MIPS34	$2.01(\pm 0.54) \times 10^{-22}$	0.02 ± 0.01	$< 1.12 \times 10^{-22}$...	$5.58(\pm 1.79) \times 10^{-23}$	$0.01 \pm 0.00^*$
MIPS39
MIPS55	$8.97(\pm 1.56) \times 10^{-22}$	0.28 ± 0.05	$5.14(\pm 1.58) \times 10^{-22}$	0.13 ± 0.04	$1.59(\pm 0.24) \times 10^{-22}$	0.04 ± 0.01	$< 1.11 \times 10^{-22}$...
MIPS168	$4.86(\pm 1.46) \times 10^{-22}$	0.96 ± 0.28	$9.68(\pm 1.57) \times 10^{-22}$	1.45 ± 0.24	$3.00(\pm 0.31) \times 10^{-22}$	0.45 ± 0.05	$< 1.30 \times 10^{-22}$...
MIPS213	$< 1.15 \times 10^{-22}$...	$< 7.08 \times 10^{-23}$...	$< 3.35 \times 10^{-23}$
MIPS224	$2.34(\pm 0.35) \times 10^{-22}$	0.13 ± 0.02	$< 7.42 \times 10^{-23}$...	$< 3.73 \times 10^{-23}$
MIPS268	$1.86(\pm 0.47) \times 10^{-22}$	0.14 ± 0.04	$< 2.01 \times 10^{-22}$...	$< 8.71 \times 10^{-23}$
MIPS277	$5.94(\pm 0.58) \times 10^{-22}$	0.49 ± 0.05	$2.84(\pm 0.78) \times 10^{-22}$	0.25 ± 0.07	$< 3.44 \times 10^{-23}$
MIPS298
MIPS324	$6.57(\pm 0.59) \times 10^{-22}$	0.64 ± 0.06	$2.66(\pm 0.57) \times 10^{-22}$	0.26 ± 0.06	$4.69(\pm 1.32) \times 10^{-23}$	0.04 ± 0.01	$7.91(\pm 1.19) \times 10^{-23}$	0.09 ± 0.01
MIPS350	$6.18(\pm 0.55) \times 10^{-22}$	0.71 ± 0.06	$4.90(\pm 0.63) \times 10^{-22}$	0.42 ± 0.05	$9.30(\pm 1.41) \times 10^{-23}$	0.07 ± 0.01	$1.03(\pm 0.13) \times 10^{-22}$	0.07 ± 0.01
MIPS358	$1.19(\pm 0.10) \times 10^{-21}$	3.35 ± 0.28	$1.24(\pm 0.07) \times 10^{-21}$	2.72 ± 0.15	$1.98(\pm 0.15) \times 10^{-22}$	0.41 ± 0.03	$5.54(\pm 1.22) \times 10^{-23}$	0.08 ± 0.02
MIPS394	$8.87(\pm 0.60) \times 10^{-22}$	3.66 ± 0.25	$9.57(\pm 0.53) \times 10^{-22}$	2.48 ± 0.14	$8.52(\pm 1.25) \times 10^{-23}$	0.21 ± 0.03	$< 5.67 \times 10^{-23}$...
MIPS397	$< 7.31 \times 10^{-23}$...	$2.14(\pm 0.40) \times 10^{-22}$	0.16 ± 0.03	$< 3.07 \times 10^{-23}$
MIPS419	$< 2.91 \times 10^{-22}$...	$< 2.32 \times 10^{-22}$...	$< 4.61 \times 10^{-23}$...	$< 4.54 \times 10^{-23}$...
MIPS472	$8.60(\pm 0.62) \times 10^{-22}$	2.17 ± 0.16	$5.14(\pm 0.62) \times 10^{-22}$	1.35 ± 0.16	$1.07(\pm 0.12) \times 10^{-22}$	0.28 ± 0.03	$< 4.17 \times 10^{-23}$...
MIPS488	$1.44(\pm 0.10) \times 10^{-21}$	2.78 ± 0.19	$6.69(\pm 1.21) \times 10^{-22}$	1.06 ± 0.19	$1.62(\pm 0.22) \times 10^{-22}$	0.26 ± 0.04	$< 4.97 \times 10^{-23}$...
MIPS512	$2.13(\pm 0.46) \times 10^{-22}$	0.31 ± 0.07	$3.00(\pm 0.53) \times 10^{-22}$	0.37 ± 0.07	$< 4.95 \times 10^{-23}$...	$5.74(\pm 1.26) \times 10^{-23}$	0.07 ± 0.02
MIPS521	$4.55(\pm 0.83) \times 10^{-22}$	1.34 ± 0.24
MIPS530	$6.61(\pm 0.76) \times 10^{-22}$	3.57 ± 0.41	$6.17(\pm 0.96) \times 10^{-22}$	2.12 ± 0.33	$7.72(\pm 1.44) \times 10^{-23}$	0.26 ± 0.05	$< 6.67 \times 10^{-23}$...
MIPS532	$< 1.58 \times 10^{-22}$...	$2.22(\pm 0.17) \times 10^{-22}$	0.10 ± 0.01	$< 9.37 \times 10^{-23}$
MIPS537	$1.54(\pm 0.07) \times 10^{-21}$	5.72 ± 0.26	$8.35(\pm 0.97) \times 10^{-22}$	2.83 ± 0.33	$3.33(\pm 0.27) \times 10^{-22}$	1.16 ± 0.09	$9.55(\pm 1.64) \times 10^{-23}$	0.24 ± 0.04
MIPS542	$5.93(\pm 0.62) \times 10^{-22}$	2.60 ± 0.27	$6.55(\pm 0.65) \times 10^{-22}$	2.96 ± 0.29	$8.98(\pm 1.23) \times 10^{-23}$	0.42 ± 0.06	$6.80(\pm 1.35) \times 10^{-23}$	0.34 ± 0.07
MIPS544	$2.53(\pm 0.53) \times 10^{-22}$	0.38 ± 0.08	$< 2.21 \times 10^{-22}$...	$< 4.68 \times 10^{-23}$...	$< 5.47 \times 10^{-23}$...
MIPS546	$1.22(\pm 0.05) \times 10^{-21}$	2.58 ± 0.11	$8.17(\pm 0.62) \times 10^{-22}$	1.37 ± 0.10	$1.57(\pm 0.12) \times 10^{-22}$	0.26 ± 0.02	$9.52(\pm 1.68) \times 10^{-23}$	0.16 ± 0.03
MIPS549	$5.70(\pm 0.67) \times 10^{-22}$	1.07 ± 0.13	$5.87(\pm 0.54) \times 10^{-22}$	1.14 ± 0.10	$6.18(\pm 1.21) \times 10^{-22}$	0.12 ± 0.02	$< 3.52 \times 10^{-23}$...
MIPS562	$1.23(\pm 0.07) \times 10^{-21}$	2.43 ± 0.14	$1.48(\pm 0.11) \times 10^{-21}$	2.52 ± 0.19	$2.44(\pm 0.30) \times 10^{-22}$	0.43 ± 0.05	$7.42(\pm 1.25) \times 10^{-23}$	0.17 ± 0.03
MIPS8040	$1.85(\pm 0.12) \times 10^{-21}$	1.22 ± 0.08	$1.05(\pm 0.11) \times 10^{-21}$	0.47 ± 0.05	$2.14(\pm 0.20) \times 10^{-22}$	0.09 ± 0.01	$< 5.96 \times 10^{-23}$...
MIPS8107	$3.63(\pm 0.48) \times 10^{-22}$	0.24 ± 0.03	$1.11(\pm 0.19) \times 10^{-22}$	0.06 ± 0.01	$5.90(\pm 0.99) \times 10^{-23}$	0.03 ± 0.01	$3.45(\pm 1.07) \times 10^{-23}$	0.02 ± 0.01
MIPS8121	$1.84(\pm 0.40) \times 10^{-22}$	0.08 ± 0.02	$2.97(\pm 0.61) \times 10^{-22}$	0.12 ± 0.02	$3.28(\pm 0.98) \times 10^{-23}$	$0.01 \pm 0.00^*$
MIPS8179	$3.97(\pm 0.81) \times 10^{-22}$	0.37 ± 0.08	$3.75(\pm 1.20) \times 10^{-22}$	0.30 ± 0.10	$< 1.21 \times 10^{-22}$...	$6.69(\pm 1.05) \times 10^{-23}$	0.05 ± 0.01
MIPS8204	$1.16(\pm 0.09) \times 10^{-21}$	1.32 ± 0.10	$9.52(\pm 0.68) \times 10^{-22}$	0.96 ± 0.07	$1.38(\pm 0.15) \times 10^{-22}$	0.13 ± 0.02	$< 3.73 \times 10^{-23}$...
MIPS8226
MIPS8251
MIPS8253	$3.55(\pm 0.47) \times 10^{-22}$	0.51 ± 0.07	$5.67(\pm 0.59) \times 10^{-22}$	0.46 ± 0.05	$6.04(\pm 1.07) \times 10^{-23}$	0.04 ± 0.01	$6.64(\pm 1.11) \times 10^{-23}$	0.05 ± 0.01
MIPS8308	$9.38(\pm 0.84) \times 10^{-22}$	1.42 ± 0.13	$6.67(\pm 1.35) \times 10^{-22}$	1.01 ± 0.20	$< 8.37 \times 10^{-23}$...	$< 6.36 \times 10^{-23}$...
MIPS8311	$6.13(\pm 0.41) \times 10^{-22}$	0.62 ± 0.04	$1.84(\pm 0.58) \times 10^{-22}$	0.15 ± 0.05	$6.41(\pm 1.19) \times 10^{-23}$	0.05 ± 0.01	$< 9.97 \times 10^{-23}$...
MIPS8325	$6.44(\pm 0.90) \times 10^{-22}$	0.86 ± 0.12	$< 6.00 \times 10^{-22}$...	$2.05(\pm 0.33) \times 10^{-22}$	0.20 ± 0.03	$8.29(\pm 1.31) \times 10^{-23}$	0.08 ± 0.01
MIPS8328	$4.82(\pm 0.69) \times 10^{-22}$	0.49 ± 0.07	$3.24(\pm 0.99) \times 10^{-22}$	0.31 ± 0.09	$7.22(\pm 1.73) \times 10^{-23}$	0.07 ± 0.02	$< 7.29 \times 10^{-23}$...
MIPS8360	$4.36(\pm 0.42) \times 10^{-22}$	0.32 ± 0.03	$4.11(\pm 0.87) \times 10^{-22}$	0.27 ± 0.06	$5.66(\pm 1.56) \times 10^{-23}$	0.04 ± 0.01
MIPS8371	$1.89(\pm 0.07) \times 10^{-21}$	7.50 ± 0.28	$1.38(\pm 0.11) \times 10^{-21}$	5.08 ± 0.40	$2.77(\pm 0.24) \times 10^{-22}$	1.06 ± 0.09	$< 1.04 \times 10^{-22}$...
MIPS8375	$8.00(\pm 0.73) \times 10^{-22}$	1.70 ± 0.16	$5.82(\pm 0.80) \times 10^{-22}$	0.83 ± 0.11	$1.04(\pm 0.13) \times 10^{-22}$	0.14 ± 0.02	$1.37(\pm 0.12) \times 10^{-22}$	0.13 ± 0.01
MIPS8377	$9.57(\pm 0.90) \times 10^{-22}$	2.97 ± 0.28	$7.74(\pm 0.91) \times 10^{-22}$	1.70 ± 0.20	$1.33(\pm 0.13) \times 10^{-22}$	0.29 ± 0.03	$9.89(\pm 1.30) \times 10^{-23}$	0.29 ± 0.04
MIPS8384	$6.13(\pm 0.53) \times 10^{-22}$	0.58 ± 0.05	$7.90(\pm 2.13) \times 10^{-23}$	0.07 ± 0.02	$6.95(\pm 1.09) \times 10^{-23}$	0.06 ± 0.01	$6.26(\pm 1.13) \times 10^{-23}$	0.06 ± 0.01
MIPS8387	$1.10(\pm 0.07) \times 10^{-21}$	2.69 ± 0.17	$5.63(\pm 0.68) \times 10^{-22}$	1.51 ± 0.18	$6.11(\pm 1.20) \times 10^{-23}$	0.17 ± 0.03	$< 4.68 \times 10^{-23}$...
MIPS8388	$7.52(\pm 0.50) \times 10^{-22}$	1.08 ± 0.07	$5.27(\pm 0.71) \times 10^{-22}$	0.67 ± 0.09	$7.09(\pm 1.24) \times 10^{-23}$	0.09 ± 0.02	$8.62(\pm 1.87) \times 10^{-23}$	0.09 ± 0.02
MIPS8392	$3.06(\pm 0.97) \times 10^{-22}$	1.58 ± 0.50
MIPS8401	$1.33(\pm 0.09) \times 10^{-21}$	3.43 ± 0.23	$1.09(\pm 0.14) \times 10^{-21}$	2.05 ± 0.26	$3.25(\pm 0.41) \times 10^{-22}$	0.60 ± 0.08	$4.94(\pm 1.29) \times 10^{-23}$	0.07 ± 0.02
MIPS8405	$5.90(\pm 0.48) \times 10^{-22}$	0.65 ± 0.05	$7.90(\pm 0.77) \times 10^{-22}$	0.80 ± 0.08	$1.69(\pm 0.11) \times 10^{-22}$	0.16 ± 0.01	$9.17(\pm 2.35) \times 10^{-23}$	0.08 ± 0.02
MIPS8411
MIPS8424	$1.04(\pm 0.20) \times 10^{-22}$	0.07 ± 0.01	$8.63(\pm 0.79) \times 10^{-22}$	0.47 ± 0.04	$< 4.80 \times 10^{-23}$
MIPS8430	$4.57(\pm 1.04) \times 10^{-22}$	1.03 ± 0.23	$< 6.53 \times 10^{-22}$...	$1.30(\pm 0.21) \times 10^{-22}$	0.19 ± 0.03	$5.25(\pm 1.43) \times 10^{-23}$	0.08 ± 0.02
MIPS8450	$1.08(\pm 0.05) \times 10^{-21}$	3.93 ± 0.18	$7.25(\pm 0.59) \times 10^{-22}$	3.23 ± 0.26	$1.15(\pm 0.12) \times 10^{-22}$	0.55 ± 0.06
MIPS8462	$2.97(\pm 0.58) \times 10^{-22}$	0.33 ± 0.06	$3.11(\pm 0.72) \times 10^{-22}$	0.28 ± 0.06	$8.91(\pm 1.16) \times 10^{-23}$	0.07 ± 0.01	$5.97(\pm 1.48) \times 10^{-23}$	0.05 ± 0.01
MIPS8477	$3.04(\pm 0.52) \times 10^{-22}$	0.38 ± 0.07
MIPS8479	$< 5.34 \times 10^{-22}$...	$4.47(\pm 0.64) \times 10^{-22}$	0.14 ± 0.02	$< 8.37 \times 10^{-23}$
MIPS8495	$< 6.20 \times 10^{-23}$...	$< 1.30 \times 10^{-22}$...	$5.40(\pm 1.11) \times 10^{-23}$	0.06 ± 0.01
MIPS8499	$1.49(\pm 0.09) \times 10^{-21}$	7.86 ± 0.47	$1.41(\pm 0.13) \times 10^{-21}$	5.55 ± 0.51	$1.94(\pm 0.33) \times 10^{-22}$	0.73 ± 0.13	$< 2.95 \times 10^{-23}$...
MIPS8507	$7.46(\pm 0.98) \times 10^{-22}$	1.33 ± 0.17	$7.54(\pm 0.87) \times 10^{-22}$	1.26 ± 0.15	$6.25(\pm 1.83) \times 10^{-23}$	0.11 ± 0.03	$< 4.89 \times 10^{-23}$...
MIPS8521	$3.55(\pm 0.42) \times 10^{-22}$	0.33 ± 0.04	$4.27(\pm 0.56) \times 10^{-22}$	0.24 ± 0.03	$< 6.17 \times 10^{-23}$...	$< 1.16 \times 10^{-22}$...
MIPS8526	$1.04(\pm 0.09) \times 10^{-21}$	2.37 ± 0.21	$4.00(\pm 0.83) \times 10^{-22}$	0.72 ± 0.15	$5.77(\pm 1.50) \times 10^{-23}$	0.10 ± 0.03	$< 6.38 \times 10^{-23}$...
MIPS8532	$4.61(\pm 0.83) \times 10^{-22}$	0.79 ± 0.14	$< 1.25 \times 10^{-22}$...	$5.80(\pm 1.66) \times 10^{-23}$	0.08 ± 0.02	$6.35(\pm 1.13) \times 10^{-23}$	0.10 ± 0.02
MIPS8543	$2.73(\pm 0.09) \times 10^{-21}$	3.19 ± 0.11	$1.83(\pm 0.15) \times 10^{-21}$	2.01 ± 0.16	$1.83(\pm 0.35) \times 10^{-22}$	0.20 ± 0.04	$< 4.81 \times 10^{-23}$...
MIPS8550	$< 9.33 \times 10^{-22}$							

TABLE 4—Continued

Galaxy (MIPS)	$f_{11.3}$ (Wcm $^{-2}$)	$EW_{11.3}$ (μm)	$f_{12.7}$ (Wcm $^{-2}$)	$EW_{12.7}$ (μm)	$f_{[NeII]}$ (Wcm $^{-2}$)	$EW_{[NeII]}$ (μm)	$f_{[NeIII]}$ (Wcm $^{-2}$)	$EW_{[NeIII]}$ (μm)
MIPS16267	$<1.78 \times 10^{-22}$...	$<2.61 \times 10^{-22}$...	$<3.95 \times 10^{-23}$
MIPS22235	$2.64(\pm 0.11) \times 10^{-21}$	1.34 ± 0.06	$2.32(\pm 0.14) \times 10^{-21}$	0.87 ± 0.05	$4.43(\pm 0.34) \times 10^{-22}$	0.15 ± 0.01	$<7.33 \times 10^{-23}$...
MIPS22307	$1.07(\pm 0.10) \times 10^{-21}$	0.69 ± 0.06	$7.92(\pm 0.99) \times 10^{-22}$	0.51 ± 0.06	$9.35(\pm 1.91) \times 10^{-23}$	0.06 ± 0.01	$8.36(\pm 1.17) \times 10^{-23}$	0.05 ± 0.01
MIPS22323	$5.59(\pm 0.51) \times 10^{-22}$	0.27 ± 0.02	$2.30(\pm 0.65) \times 10^{-22}$	0.12 ± 0.03	$1.03(\pm 0.14) \times 10^{-22}$	0.06 ± 0.01
MIPS22352	$2.07(\pm 0.10) \times 10^{-21}$	2.83 ± 0.14	$1.23(\pm 0.15) \times 10^{-21}$	1.47 ± 0.18	$1.76(\pm 0.21) \times 10^{-22}$	0.21 ± 0.03	$6.19(\pm 1.23) \times 10^{-23}$	0.06 ± 0.01
MIPS22356	$3.92(\pm 0.44) \times 10^{-22}$	0.20 ± 0.02	$3.34(\pm 0.64) \times 10^{-22}$	0.15 ± 0.03	$5.96(\pm 1.25) \times 10^{-23}$	$0.02 \pm 0.00^*$	$7.05(\pm 1.70) \times 10^{-23}$	0.03 ± 0.01
MIPS22371	$4.66(\pm 0.36) \times 10^{-22}$	0.26 ± 0.02	$1.94(\pm 0.38) \times 10^{-22}$	0.11 ± 0.02	$<5.94 \times 10^{-23}$
MIPS22379	$5.00(\pm 0.77) \times 10^{-22}$	0.44 ± 0.07	$1.50(\pm 0.46) \times 10^{-22}$	0.12 ± 0.04	$<6.03 \times 10^{-23}$...	$4.40(\pm 1.10) \times 10^{-23}$	0.03 ± 0.01
MIPS22417
MIPS22432	$5.37(\pm 0.33) \times 10^{-22}$	0.54 ± 0.03	$<4.25 \times 10^{-22}$...	$1.69(\pm 0.19) \times 10^{-22}$	0.08 ± 0.01
MIPS22536	$4.09(\pm 0.58) \times 10^{-22}$	0.27 ± 0.04	$7.58(\pm 0.87) \times 10^{-22}$	0.34 ± 0.04	$<5.42 \times 10^{-23}$
MIPS22549	$3.53(\pm 0.59) \times 10^{-22}$	0.38 ± 0.06	$3.00(\pm 0.79) \times 10^{-22}$	0.32 ± 0.08	$<2.99 \times 10^{-23}$
MIPS22555	$<2.38 \times 10^{-22}$
MIPS22557	$6.40(\pm 1.58) \times 10^{-22}$	1.13 ± 0.28	$7.66(\pm 1.34) \times 10^{-22}$	1.24 ± 0.22	$<7.04 \times 10^{-23}$...	$6.57(\pm 1.67) \times 10^{-23}$	0.08 ± 0.02
MIPS22635	$6.51(\pm 0.99) \times 10^{-22}$	1.58 ± 0.24	$5.69(\pm 0.96) \times 10^{-22}$	0.93 ± 0.16	$7.41(\pm 1.54) \times 10^{-23}$	0.11 ± 0.02	$4.35(\pm 1.13) \times 10^{-23}$	0.06 ± 0.02
MIPS22638	$2.96(\pm 0.57) \times 10^{-22}$	0.38 ± 0.07	$3.18(\pm 0.63) \times 10^{-22}$	0.36 ± 0.07	$<3.93 \times 10^{-23}$...	$5.28(\pm 1.27) \times 10^{-23}$	0.05 ± 0.01
MIPS22690
MIPS22722

NOTE.— Fluxes may not be given for lines that are in the IRS wavelength range when their neighboring continuum cannot be well determined.

* Error bars of 0 correspond to EW uncertainties that are lower than the selected measurement accuracy.

REFERENCES

- Adelberger, K. L., Steidel, C. C., Shapley, A. E., Hunt, M. P., Erb, D. K., Reddy, N. A., & Pettini, M. 2004, ApJ, 607, 226
- Allamandola, L. J., Hudgins, D. M., & Sandford, S. A. 1999, ApJ, 511, L115
- Alexander, D. M., et al. 2008, AJ, 135, 1968
- Armus, L., et al. 2006, ApJ, 640, 204
- Armus, L., et al. 2007, ApJ, 656, 148
- Barger, A. J., Cowie, L. L., & Wang, W.-H. 2008, ApJ, 689, 687
- Barmby, P., et al. 2006, ApJ, 642, 126
- Bertin, E., & Arnouts, S. 1996, A&AS, 117, 393
- Brand, K. et al. 2008, ApJ, 680, 119
- Brandl, B. R. et al. 2006, ApJ, 653, 1129
- Cardamone, C. N., et al. 2008, ApJ, 680, 130
- Carilli, C. L. et al. 2005, ApJ, 618, 586
- Chary, R., & Elbaz, D. 2001, ApJ, 556, 562
- Chiar, J. E. & Tielens, A. G. G. M. 2006, ApJ, 637, 774
- Conselice, C. J. 2006, ApJ, 638, 686
- Daddi, E., et al. 2004, ApJ, 600, L127
- Daddi, E., et al. 2005, ApJ, 631, L13
- Dale, D. A. et al. 2006, ApJ, 646, 161
- Dasyra, K. M., Yan, L., Helou, G., Surace, J., Sajina, A., & Colbert, J. 2008, ApJ, 680, 232
- Dasyra, K. M., et al. 2008, ApJ, 674, L9
- Dey, A. et al. 2008, ApJ, 677, 943
- Dey, A., et al. 2009, ASPC, in press, arXiv/0905.4531
- Desai, V., et al. 2007, ApJ, 669, 810
- Desai, V., et al. 2009, ApJ, in press, arXiv/0905.4274
- Donley, J. L., Rieke, G. H., Prez-Gonzlez, P. G., Rigby, J. R., & Alonso-Herrero, A. 2007, ApJ, 660, 167
- Draine, B. T., & Lee, H. M. 1984, ApJ, 402, 441
- Draine, B. T., & Li, A. 2007, ApJ 657, 810
- Fadda, D., et al. 2004, AJ, 128, 1
- Fadda, D., et al. 2006, AJ, 131, 2859
- Farrah, D., et al. 2007, ApJ, 667, 149
- Farrah, D., et al. 2008, ApJ, 677, 957
- Farrah, D., et al. 2009, ApJ, in press, arXiv/0905.1956
- Frayer, D. T., et al. 2006, AJ, 131, 250
- Galliano, F., Madden, S. C., Tielens, A. G. G. M., Peeters, E., & Jones, A. P. 2008, ApJ, 679, 310
- Genzel, R., et al. 1998, ApJ, 498, 579
- Georgantopoulos, I., Georgakakis, A., & Akylas, A. 2007, A&A, 466, 823
- Gorjian, V. et al. 2008, ApJ, 679, 1040
- Hammer, F., Flores, H., Elbaz, D., Zheng, X. Z., Liang, Y. C., & Cesarsky, C. 2005, A&A, 430, 115
- Hernán-Caballero, A. et al. 2009, MNRAS, in press, arXiv/0902.3369
- Higdon, S. J. U., Armus, L., Higdon, J. L., Soifer, B. T., & Spoon, H. W. W. 2006, ApJ, 648, 323
- Higdon, J. L., Higdon, S. J. U., Willner, S. P., Brown, M. J. I., Stern, D., Le Floc'h, E., & Eisenhardt, P. 2008, ApJ, 688, 885
- Houck, J. R., et al. 2005, ApJ, 622, L105
- Huang, J.-S., et al. 2009, ApJ, in press, arXiv/0904.4479
- Imanishi, M. 2002, ApJ, 569, 44
- Imanishi, M., Dudley, C. C., & Maloney, P. R. 2006, ApJ, 637, 114
- Imanishi, M., Nakagawa, T., Ohyama, Y., Shirahata, M., Wada, T., Onaka, T., & Oi, N. 2008, PASJ, 60, 489

- Kartaltepe, J. S., et al. 2007, ApJS, 172, 320
- Komossa, S., Burwitz, V., Hasinger, G., Predehl, P., Kaastra, J. S., & Ikebe, Y. 2003, ApJ, 582, L15
- Lacy, M., et al. 2004 ApJS, 154, 166
- Lacy, M., et al. 2005 ApJS, 161, 41
- Lacy, M., Petric, A. O., Sajina, A., Canalizo, G., Storrie-Lombardi, L. J., Armus, L., Fadda, D., & Marleau, F. R. 2007, AJ, 133, 186
- Le Floc'h, E., et al. 2005, ApJ, 632, 169
- Martinez-Sansigre, A., Lacy, M., Sajina, A., & Rawlings, S. 2008, ApJ, 674, 676
- Melbourne, J., et al. 2009, AJ, in press, arXiv/0904.1231
- Menéndez-Delmestre, K., et al. 2007, ApJ, 655, L65
- Menéndez-Delmestre, K., et al. 2009, ApJ, in press, arXiv/0903.4017
- Papovich, C., et al. 2004, ApJS, 154, 70
- Papovich, C., et al. 2006, ApJS, 640, 92
- Peeters, E., Spoon, H. W. W., & Tielens, A. G. G. M. 2004, ApJ, 613, 986
- Peng, C. Y., Ho, L. C., Impey, C. D., & Rix, H.-W. 2002, AJ, 124, 266
- Pérez-González, P. G., et al. 2005, ApJ, 630, 82
- Polletta, M. et al. 2006, ApJ, 642, 673
- Polletta, M. et al. 2007, ApJ, 663, 81
- Pope, A., et al. 2008, ApJ, 675, 1171
- Rigby, J. R., et al. 2004, ApJS, 154, 160
- Rigopoulou, D., Spoon, H. W. W., Genzel, R., Lutz, D., Moorwood, A. F. M., & Tran, Q. D. 1999, AJ, 118, 2625
- Rigopoulou, D., Kunze, D., Lutz, D., Genzel, R., & Moorwood, A. F. M. 2002, A&A, 389, 374
- Risaliti, G. et al. 2006, MNRAS, 365, 303
- Sajina, A., Yan, L., Armus, L., Choi, P., Fadda, D., Helou, G., & Spoon, H. 2007, ApJ, 664, 713
- Sajina, A., et al. 2008, ApJ, 683, 659
- Sanders, D. B., Soifer, B. T., Elias, J. H., Madore, B. F., & Matthews, K. 1988, ApJ, 328, L35
- Solomon, P. M., & Vanden Bout, P. A. 2005, ARA&A, 43, 677
- Smith, J. D. T., et al. 2007, ApJ, 656, 770
- Steidel, C. C., Shapley, A. E., Pettini, M., Adelberger, K. L., Erb, D. K., Reddy, Naveen A., & Hunt, Matthew P. 2004, ApJ, 604, 534
- Stern, D., et al. 2005, ApJ, 631, 163
- Sturm, E., Lutz, D., Tran, D., Feuchtgruber, H., Genzel, R., Kunze, D., Moorwood, A. F. M., & Thornley, M. D. 2000, A&A, 358, 481
- Sturm, E., Lutz, D., Verma, A., Netzer, H., Sternberg, A., Moorwood, A. F. M., Oliva, E., & Genzel, R. 2002, A&A, 393, 821
- Surace, J., et al. 2005, "The SWIRE data release 2: Image atlases and source catalogs for ELAIS-N1, ELAIS-N2, XMM-LSS, and the Lockman Hole"
- Swinbank, A. M., Chapman, S. C., Smail, I., Lindner, C., Borys, C., Blain, A. W., Ivison, R. J., & Lewis, G. F. 2006, MNRAS, 371, 465
- Tacconi, L. J., et al. (2006) 2006, ApJ, 640, 228
- Valiante, E., Lutz, D., Sturm, E., Genzel, R., Tacconi, L. J., Lehnert, M. D., & Baker, A. J. 2007, ApJ., 660, 1060
- Veilleux, S., et al. 2006, ApJ, 643, 707
- Verma, A., Lutz, D., Sturm, E., Sternberg, A., Genzel, R., & Vacca, W. 2003, A&A, 403, 829
- Weedman, D. W., Le Floc'h, E., Higdon, S. J. U., Higdon, J. L., & Houck, J. R. 2006, ApJ, 638, 613
- Weedman, D. W. & Houck, J. R. 2008, ApJ, 686, 127
- Yan, H., et al. 2004, ApJ, 616, 63
- Yan, L., et al. 2004, ApJS, 154, 75
- Yan, L., et al. 2005, ApJ, 628, 604

Yan, L., et al. 2007, ApJ, 658, 778

Yun, M. S., et al. 2008, MNRAS, 389, 333

Zheng, X. Z., Hammer, F., Flores, H., Assémat,
F., & Pelat, D. 2004, A&A, 421, 847